Norwegian University of
Science and Technology

X-ray diffraction studies of InAs/GaAs heterostructures

Arnt Joakim Wrålsen

Master of Science in Electronics
Submission date: February 2012
Supervisor: Bjørn-Ove Fimland, IET
Co-supervisor: Turid Reenaas, IFY

Norwegian University of Science and Technology
Department of Electronics and Telecommunications

Problem Description

Self-organized InAs/GaAs quantum dots (QDs) can be used for the realization of so-called intermediate band solar cells (IBSC), since the quantized energy levels in the InAs QDs can form an intermediate energy band in the bandgap of the surrounding GaAs material. Even though the InAs/GaAs QD material system has been studied since the 1980s, several aspects of the QD growth are not completely established. One example is the thickness of the 2D InAs wetting layer (WL) that is formed in the first step of the self-organized growth, and that later may be eroded as the QDs form and increase in size. The WL may also be modified as the QDs and the WL is overgrown (capped) with GaAs.

One method that could be used to estimate the thickness of the final WL is X-ray diffraction (XRD); a non-destructive technique extensively used to characterize semiconductor hetero-structures and multilayers. Information about layer thickness, superlattice period and composition can be extracted, by comparing the measured XRD curve with a simulated one. However, XRD is rarely used to characterize the layer structure of QD materials. This master thesis thus consists of two main parts:

A) Experimental work to determine the InAs and GaAs layer thicknesses in an InAs/GaAs bilayer QD sample.

B) Theoretical work to evaluate what kind of fine structure in the composition of the bilayer sample can be detected by XRD.

For the first part, the student should:

1) Perform XRD measurements at IET on an InAs/GaAs bilayer QD sample to see if such measurements give data of high enough quality/resolution. The sample to study has been grown using Molecular Beam Epitaxy (MBE), but without rotation of the substrate during the deposition. When the substrate is not rotated, a gradient of the amount of deposited material is expected. The XRD data should be recorded for several locations on the sample.

2) Estimate the variation on deposited amount of InAs and GaAs across the sample, based on the geometry of the MBE machine at IET.

3) Using the LEPTOS software for the XRD instrument at IET, perform simulations of rocking curve scans around the 004 reflection from an InAs/GaAs bilayer QD structure, and by varying the thickness of the InAs and GaAs layers in the simulation and compare to experimental data, determine how the GaAs and InAs film thicknesses vary across the sample.

In the second part, the student should model various cases of how the InAs material could be distributed in the sample. During growth of the initial 2D WL, intermixing may occur, and during capping, segregation may take place. Both these effects may result in an alloying of the InAs and the GaAs. Also it is unclear whether ALL the InAs, i.e. both in the 2D WL and in the 3D QDs, will contribute to the rocking curve scans or if only the 2D WL contributes.

The different model cases should then be simulated with LEPTOS, to evaluate what kind of alloying and what variations in the bilayer structure could give significant enough differences in the XRD curves that it might be detectable in analysis of XRD from real samples.

Assignment given: 26 June 2011
Supervisor: Bjørn-Ove Fimland, IET
Co-supervisor: Turid Reenaas, IFY

Preface

This thesis was written autumn/winter 2011–2012 thanks to the help from among others the members of the QD-IBSC group (a collaboration between the Department of Electronics and Telecommunications and the Department of Physics at NTNU, Norway).

My thanks goes to Bjørn-Ove Fimland and Turid Worren Reenaas for their help and feedback during my work with this thesis, to Maryam Gholami Mayani and Sedsel Fretheim Thomassen for growing the MBE sample and to Saroj Kumar Patra and Magnus Breivik for their help and support in using the XRD machine.

Abstract

Intermediate band solar cells (IBSC) is a proposed new type of solar cell device that has an intermediate energy band in the band gap. One possible implementation of IBSCs is by using arrays of nano-sized semiconductor particles known as quantum dots (QDs). InAs QDs can be grown on GaAs by using molecular beam epitaxy (MBE). As a part of this growth process, an InAs wetting layer (WL) is formed on which the InAs QDs grow. One possible method of determining the WL thickness is by using x-ray diffraction (XRD), which is a non-destructive analysis technique used to extract information about the structure and composition of crystalline thin films.

An InAs/GaAs bilayer sample grown by MBE was investigated. This sample was grown without rotation, meaning the thicknesses of the deposited layers are expected to exhibit a gradient across the sample. Based on the geometry of the MBE machine, the variation in deposited thicknesses across the sample was estimated to be $\pm 3.4\%$ for InAs and $\pm 4.2\%$ for GaAs. XRD rocking curve measurements were performed around the 004 reflection in thirteen different locations on this sample. LEPTOS software was used to simulate XRD curves, and these simulations were fitted to the XRD measurements by varying the thicknesses of the simulated InAs and GaAs layers. It was found that the GaAs thicknesses across the sample varied as expected, while the variation in InAs thicknesses was much larger than expected. It was also found that the measured thicknesses of the InAs layer were significantly thinner than the nominal value. This is a strong indication that there are QDs on the sample, and that only the WL of the QDs contributes to the x-ray curve.

LEPTOS was also used to simulate several cases of alloying of an InAs/-GaAs bilayer. It was found that if the entire InAs layer is segregated into an InAs/GaAs alloy, this causes the diffraction peaks to weaken as the InAs/-GaAs interfaces become less abrupt. It was also found that intermixing causes a significant change in the XRD curve because the amount of GaAs in the InAs/GaAs bilayer structure increases.

Contents

1 Introduction **1**

2 Theory **3**
2.1 Semiconductors . . . 3
2.1.1 The Fermi level . . . 5
2.1.2 p-n junctions . . . 6
2.2 Solar cells . . . 7
2.3 Intermediate band solar cells . . . 10
2.4 Quantum Dots . . . 10
2.4.1 Quantum dot growth . . . 12
2.5 Quantum dot intermediate band solar cells . . . 13
2.6 Crystal lattices . . . 14
2.6.1 Crystal planes . . . 17
2.6.2 Monolayers . . . 18
2.6.3 Strain . . . 19
2.7 X-ray diffraction . . . 19
2.7.1 Plane waves . . . 19
2.7.2 Bragg's law . . . 22
2.7.3 X-rays and x-ray diffraction . . . 23
2.7.4 Superlattices . . . 23

3 Experimental methodology **27**
3.1 Molecular beam epitaxy . . . 27
3.1.1 Deposition thickness as a function of the location on the sample . . . 30
3.2 X-ray diffraction . . . 32

4 Simulations **35**
4.1 MBE flux simulation . . . 35
4.2 X-ray diffraction simulations . . . 38
4.2.1 GaAs spacer thickness . . . 40

4.2.2 InAs layer thicknesses 44
4.2.3 Segregation 58
4.2.4 Intermixing and segregation 68
4.2.5 Summary 72

5 X-ray diffraction measurements 73
5.1 Measurement results 73
5.2 Curve fitting 77
5.3 Estimated superlattice thickness 83
5.4 Discussion 85

6 Conclusion 87

Bibliography 90

A Appendix 91
A.1 Source code for wafer flux simulations 91

Chapter 1

Introduction

In 1961 Shockley and Queisser calculated the theoretical limit of the conversion efficiency for current semiconductor solar cells to be 40.7% [1], meaning that they can covert no more than 40.7% of the energy in sunlight to electric energy. If solar cells are to exceed this limit, new technologies have to be developed and implemented.

One important limitation of solar cells is the band gap of the semiconductor. The solar cell can not absorb photons with energies lower than the band gap. Photons with energies much larger than the band gap are absorbed, albeit with large energy losses. This means that optimum energy conversion only happens for photons with energies equal to or slightly larger than the band gap of the solar cell semiconductor material. As the solar light consists of a broad spectrum of photon energies, this means that large parts of the energy in the solar spectrum is lost.

Intermediate band solar cells (IBSCs) is a proposed new type of solar cell device where this limitation is circumvented by inserting an extra energy band in the band gap[2]. This means that the band gap of the semiconductor is in practice divided into two smaller band gaps. These two smaller band gaps make it possible to absorb lower energy photons. The original band gap also still exists, meaning that relatively high energy photons can be efficiently absorbed. Luque and Martí showed in 1997 that the maximum theoretical efficiency for IBSCs is 63.1% [2] as compared to 40.7% which is the Shockley-Queisser limit mentioned above.

Several possible ways of realising IBSCs have been investigated. One of them is based on the implementation of arrays of nano-sized semiconductor particles known as *quantum dots* (QDs)[3]. A number of requirements must be fulfilled for this quantum dot array to give rise to the desired intermediate band, including high density, regular size and regular spacing [4]. At NTNU there is a research group (the QD-IBSC group, a collaboration between the

Department of Electronics and Telecommunications and the Department of Physics) which is currently investigating InAs quantum dots grown on a GaAs substrate by *molecular beam epitaxy* (MBE, a method of epitaxial growth of thin films), to see how the various MBE growth parameters affect the quantum dot properties.

X-ray diffraction is used to investigate the properties of crystalline thin films, but has not been used at NTNU on QD materials until now. This technique has been used by others to investigate InAs/GaAs heterostructures with quantum dots. See for example [5].

The purpose of this thesis is to study InAs/GaAs heterostructures with x-ray diffraction, through simulations and diffraction measurements on a sample with a InAs/GaAs QD bi-layer grown by MBE. Also different cases of intermixing and segregation of an InAs layer with surrounding GaAs layers will be investigated through XRD simulations.

Chapter 2

Theory

In this chapter the theoretical background of this thesis is presented. In section 2.1 the basic theory of semiconductors is presented, and in section 2.2 solar cells are presented. In section 2.3 semiconductor and solar cell theory is used to describe the intermediate band solar cell. Quantum dots are then presented in section 2.4, and this is followed by a presentation of the quantum dot intermediate band solar cell in section 2.5. Basic crystallography is presented in section 2.6, and finally the basic theory of x-ray diffraction is presented in section 2.7.

2.1 Semiconductors

The contents of this section is taken mostly from [6].

In a given solid, there is a number of available energy states for electrons. Every energy state can be occupied by maximum two electrons where one is in the spin up and the other one is in the spin down state. Electrons that are in the outer shell of the atoms in a solid are called *valence electrons*. These electrons take part in the bonding of the atoms in the solid. The energies of valence electrons form a continuous energy *band* that is called the *valence band*. Likewise, the energies of electrons that are free to move around in the solid form a continuous energy band called the *conduction band*. If an electric current is going to flow through the solid the electrons have to be free to move around in the solid, meaning that there must be electrons available in the conduction band.

Electrons can be *excited* from the valence band to the conduction band by absorbing energy from the surroundings, e.g. thermal or optical energy.

Solids can be divided in three categories depending on how easily they conduct currents, as shown in figure 2.1.

- *Insulators* are solids with a large energy gap between the valence and the conduction bands. The energy gap has no available states for electrons. Due to the energy gap there are very few electrons in the conduction band, meaning that even for relatively high voltages, an insulator conducts a negligible current. See figure 2.1a.

- *Metals* are solids where the valence and conduction bands either overlap or are only partially filled, see figure 2.1b. This means that the conduction band is always partially filled with electrons. In other words metals will conduct a large current even at relatively small voltages.

- *Semiconductors* are similar to insulators except that the energy gap is smaller, as shown in figure 2.1c. Due to the small band gap electrons can be easily excited from the valence band to the conduction band through thermal or optical energy. This means that at room temperature there will be a certain number of electrons that have been excited thermally into the conduction band, and the semiconductor will typically have conducting properties somewhere between a metal and an insulator.

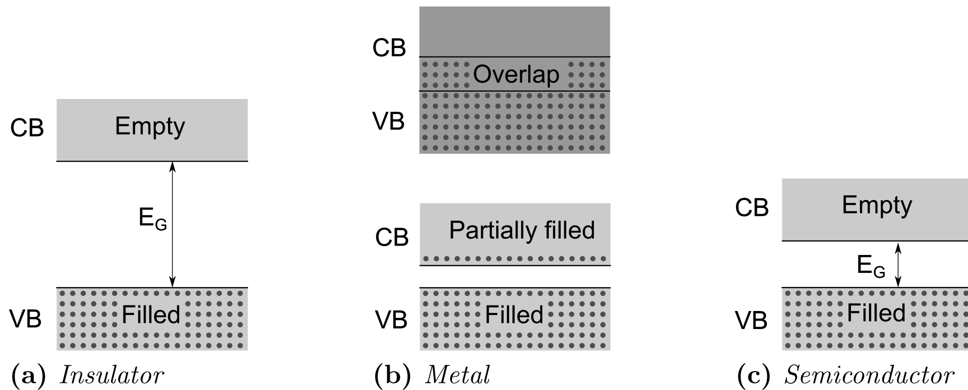

(a) *Insulator* **(b)** *Metal* **(c)** *Semiconductor*

Figure 2.1: *The electronic band diagrams of various solids at 0 K. CB is the conduction band and VB is the valence band of the solid.*

When an electron is excited from the valence band, it leaves behind an empty state. In solid state physics, this empty valence state is often modelled as a *hole*, or a positively charged particle (as opposed to electrons, which are negatively charged particles). This does not mean that holes are actual physical particles, only that they are modelled this way for simplicity. When an electron moves from a state to another inside the valence band, it fills a hole while leaving behind a new hole. This is modelled as the hole "moving around" in the valence band.

2.1.1 The Fermi level

Electrons tend to occupy the lowest energy level that is not already occupied by other electrons. This means that in a semiconductor material all the lower energy levels tend to be occupied by electrons while the higher levels are unoccupied. At the temperature of 0 K there is a sharp distinction between the completely filled and the unfilled energy levels. However, when the temperature increases, the thermal energy absorbed by electrons will cause them to be excited to higher energy levels. This means that the lower energy levels start to empty and the higher levels start to fill.

This behaviour can be described using the *Fermi-Dirac distribution function*: $f(E) = 1/(1 + e^{(E-E_F)/kT})$. Here $f(E)$ is the probability that an energy state at a given energy E is occupied by an electron. E_F is the Fermi level (a variable depending on the properties of the semiconductor) where the probability of occupation is exactly 50%, $k = 8.62 \cdot 10^{-5}$ eV K^{-1} is the Boltzmann constant and T is the temperature.

The Fermi-Dirac distribution is presented graphically in figure 2.2. Here the distribution at 0 K is shown as a black line. As can be seen, all energy states are filled below the Fermi level E_F, and all states are empty above. When the temperature increases, electrons near the Fermi level are excited thermally to higher energies and leave behind empty states. This leads to the curve being smoothed, as shown by the grey lines in the figure.

The Fermi level can be modified through the *doping* of the semiconductor, i.e. voluntarily adding impurities to the semiconductors. If elements from column V in the periodic table (so-called *donors*) is added to the semiconductor, extra electrons are added to the semiconductor (called *n-doping*). This causes the Fermi level to increase. If on the other hand elements from column III (so-called *acceptors*) are added, extra holes are added to the semiconductor and the Fermi level decreases (called *p-doping*).

When the population of charge carriers is changed from the equilibrium value through the injection of excess carriers (e.g. through the optical excitation of electron-hole pairs) the Fermi level does not give a meaningful description of the distribution of charge carriers any more. In stead, so-called quasi-Fermi level are used, with separate Fermi levels F_n and F_p for electrons and holes. The quasi-Fermi levels are defined using the equations $n = n_i e^{(F_n - E_i)/kT}$ and $p = n_i e^{(E_i - F_p)/kT}$ where n and p are the resulting steady state concentrations of electrons and holes, n_i is the intrinsic concentration of electrons excluding the excess carriers, E_i is the intrinsic Fermi level and T is the temperature.

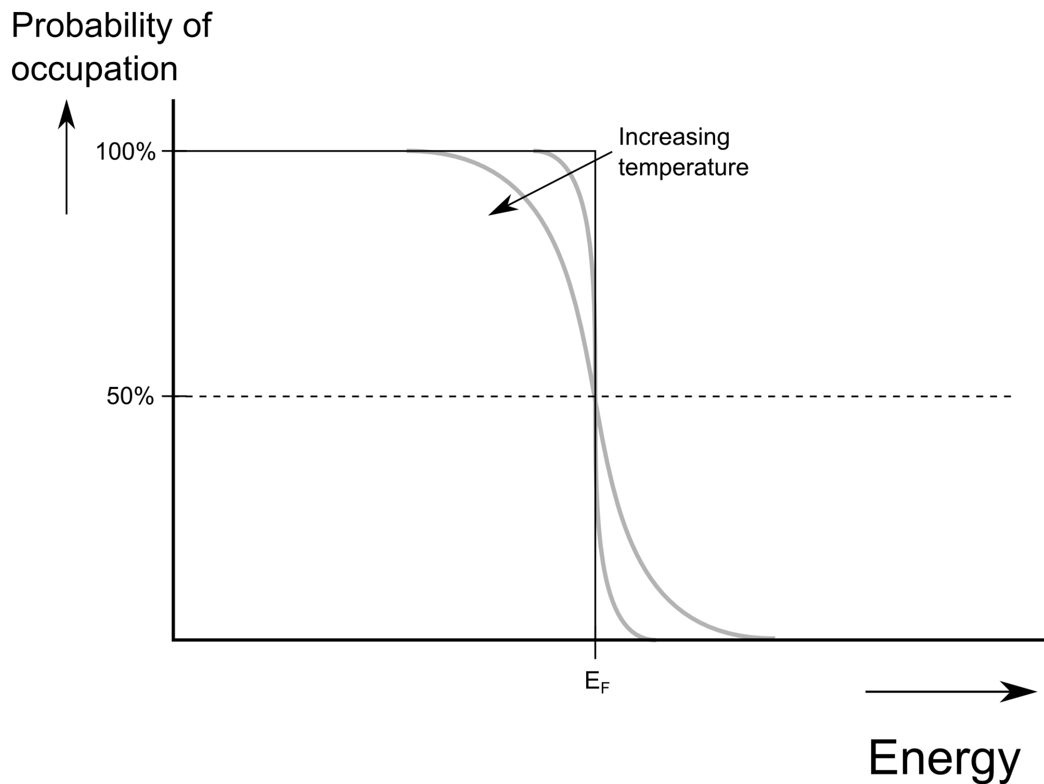

Figure 2.2: *A graphic representation of the Fermi-Dirac distribution. The probability of the energy states being occupied is shown as a function of the energy. The black line shows the distribution at 0 K. As the temperature increases, the grey lines depicts how the distribution changes.*

2.1.2 p-n junctions

A solar cell is essentially a p-n junction under illumination. In order to understand such junctions between p-doped and n-doped regions in a semiconductor, one can compare them to two separate pieces of semiconductor materials where one is p-doped and the other is n-doped. When a p-n junction is formed, a transition region arises where holes diffuse from the p side into the n side and electrons diffuse from n to p. The resulting electric band structure is shown in figure 2.3b. As shown in the figure, an electric potential arises in the transition region which leads to a gradient in the band gap figure. The difference between the conduction band top at the p-side and the n-side is called the built-in potential at equilibrium, qV_0.

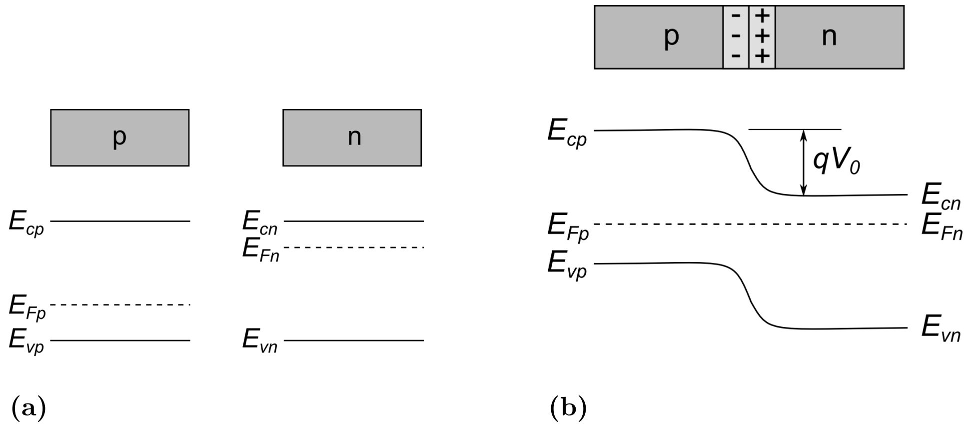

Figure 2.3: *A p-n junction at equilibrium. (a) Two separate p-doped and n-doped semiconductors together with their respective band diagram. (b) A p-n junction. Here a transition region builds up at the junction area. The built-in potential at equilibrium is shown as* V_0.

2.2 Solar cells

A solar cell (also called a *photovoltaic cell*) is a p-n junction device that converts sunlight into electrical energy. This is accomplished through the optical excitation of electrons from the valence band into the conduction band and the subsequent separation of charge carriers (also called the *photovoltaic effect*).

Light is a type of *electromagnetic radiation*, and consists of photons, which are massless particles with frequency and wavelength defined as $c = f\lambda$ where $c \approx 2.998 \cdot 10^8$ m/s is the speed of light in vacuum, f is the frequency and λ is the wavelength of the photon.

Photons incident on the solar cell can be 1) absorbed, 2) reflected, or 3) transmitted through the semiconductor. The amount of photons that are absorbed depends on properties such as band gap and cell thickness.

In chapter 13 in [7] the equation for the energy of the photon is presented as $E = hc/\lambda$, where $h = 6.63 \cdot 10^{-34}$ J s is the Planck constant, $c = 3.00 \cdot 10^{-8}$ m s^{-1} is the speed of light in vacuum, and λ is the wavelength of the photon. From this equation it can be seen that the energy of the photon is inversely proportional to the wavelength of the photon. The band gap energy ε_G of the semiconductor limits the absorption of photons. If the energy of the photon is smaller than the band gap energy (i.e. if the wavelength of the photon is too long), the photon's energy is insufficient to excite the electron from the valence band to the conduction band, and so the photon is not absorbed. In other words, the wavelength of the photon must

be equal to or lower than a maximum value determined by the band gap of the semiconductor if the photon is to be absorbed.

In figure 2.4 the band diagram of the photovoltaic cell is shown along with various energy loss mechanisms. When the electron is excited from the valence to the conduction band and a hole is created in the valence band, the part of the excitation energy used to excite the electron inside the energy bands is rapidly lost to the lattice as thermal vibrations. The larger the excitation energy is compared to the band gap energy, the more significant this energy loss becomes. More energy is lost as the electron drifts across the junction and towards the n-side contact as it drops to the n-side contact potential. In addition, wherever electrons and holes are present at the same time and place, they can recombine. The excess energy can be released either as radiation or non-radiatively.

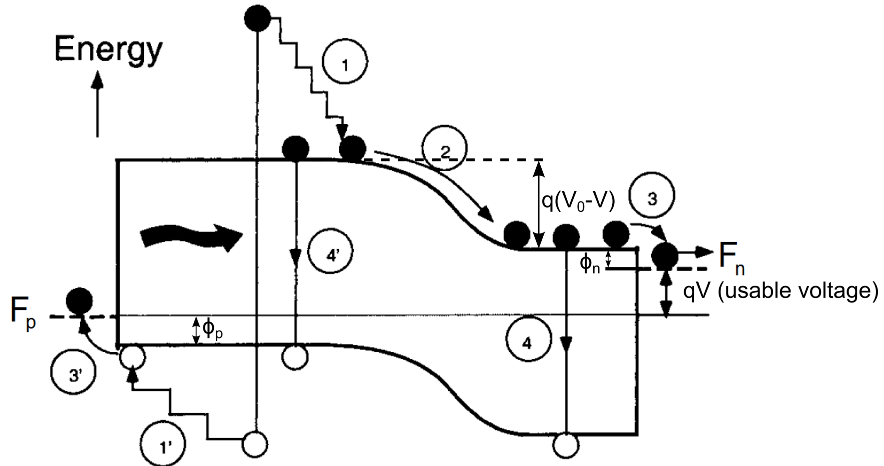

Figure 2.4: *Energy band diagram of a photovoltaic cell. Four types of electron energy losses are shown: 1) Thermal loss, 2) and 3) junction and contact voltage loss, 4) recombination loss. The corresponding losses for holes are shown as 1', 3' and 4'. Note that $\phi_n + \phi_p + q(V_0 - V) + qV = \phi_n + \phi_p + qV_0 = E_g/q$, as seen in the figure. The figure is taken from [8] and slightly modified.*

As extra electron-hole pairs are generated through optical absorption the electron and hole concentrations deviate from the equilibrium values and separate quasi-Fermi levels for electrons and holes arise. As seen in figure 2.4, electrons exiting on the n-side contact have energies equivalent to the quasi Fermi level for electrons F_n, while electrons that arrive on the p-side contact and recombine with holes in the semiconductor have energies equivalent to F_p. In other words the usable potential is the difference between F_n and F_p, and the voltage over the cell is expressed as $V = (F_n - F_p)/q$.

Figure 2.5 shows the current-voltage characteristics for a solar cell under illumination. The maximum voltage (equivalent to the open-circuit voltage) $V_{max} = V_{oc}$ is shown in the figure. At this voltage there is no current. On the other hand, the maximum current I_{max} is the same as the short-circuit current I_{sc} where the voltage over the solar cell is zero.

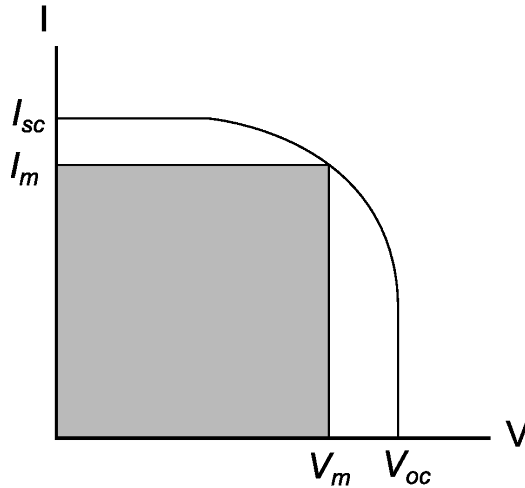

Figure 2.5: *A sketch of the current-voltage characteristics of an illuminated solar cell. The maximum power rectangle is seen as a grey box.*

As seen from figure 2.4, the maximum (open-circuit) voltage must be lower than the built-in junction voltage V_0. The built-in voltage is again lower than the energy gap voltage E_g/q. In mathematical terms, this can be expressed as $V_{max} = V_{oc} < V_0 < E_g/q$, see figure 2.4. In other words, the energy gap determines an upper limit for the maximum voltage of the solar cell. If the energy gap of the solar cell was minimized in order to absorb as much as possible of the solar spectre, the voltage would be so small that it would be necessary to connect many solar cell devices in series to create a usable output voltage. This is not a practical way of manufacturing solar cells. This means that to create a usable solar cell device, a balance must be found between minimizing the energy gap to absorb as much as possible solar light, and maximizing the energy gap to increase the output voltage of the device.

Often the output efficiency of solar cells is measured as the ratio of the maximum output power and the input power from the incident solar light: $\eta = V_m I_m / P_{in}$ [9].

To sum up, the two most important causes of energy losses in solar cells are 1) the loss of photons with energy lower than the band gap energy and 2) the loss of photons with energy higher than the band gap energy of the

semiconductor, as they are either not absorbed or absorbed with large energy losses. Decreasing the band gap would lead to a higher absorption rate of photons, but would also lead to the output voltage of the solar cell being decreased.

2.3 Intermediate band solar cells

One way of reducing energy losses in the photovoltaic cell is by inserting an extra energy band in the band gap, as shown in figure 2.6. This results in an intermediate band solar cell (IBSC). In the IBSC there are three possible excitation paths for the electrons. In addition to being excited directly from the valence to the conduction band (across the main band gap ε_G), electrons can be excited from the valence band to the intermediate band or from the intermediate band to the conduction band (excitation paths ε_H and ε_L, respectively). Now the energy of the band gap ε_G can be increased without losing the lower energy photons as the absorbed energy can be used to excite electrons over ε_L or ε_H instead. The two smaller band gaps (ε_H and ε_L) can have different magnitudes to match different parts of the solar spectrum.

2.4 Quantum Dots

Quantum dots can be used to form the intermediate band. In order to understand the concept of quantum dots it is necessary to have a look at the quantum mechanical description of confined particles (e.g. electrons). The time-independent Schrödinger equation used for modelling particles in a given potential is described in [11]: $-(\hbar^2/2m)\nabla^2\psi(\mathbf{r}) + U(\mathbf{r})\psi(\mathbf{r}) = E\psi(\mathbf{r})$. Here $\hbar = h/2\pi$ is the reduced Planck constant, m denotes the mass of the confined particle, $U(\mathbf{r})$ is the confining potential, ψ is the wavefunction of the particle, and E is the corresponding energy of the particle. This equation is used for calculating the wave function of a particle in a known potential.

A quantum dot is a structure where an electron is confined to nanoscale dimensions in all directions. As an example a cubic quantum dot can be studied. For simplicity, it will be assumed that the quantum dot has dimensions l, a potential of zero inside the dot, and an infinite potential outside. This means that the boundary values of the wave function is zero at the edges (where the infinite potential outside starts). Here the solution of the Schrödinger equation is $\psi = (l/2)^{\frac{3}{2}} \sin((n_x\pi/l)x)\sin((n_y\pi/l)y)\sin((n_z\pi/l)z)$ with the corresponding energy states $E = (\hbar^2\pi^2/2ml^2)(n_x^2 + n_y^2 + n_z^2)$ where n_x, n_y and n_z are three independent integers (see chapter 3 in [12]).

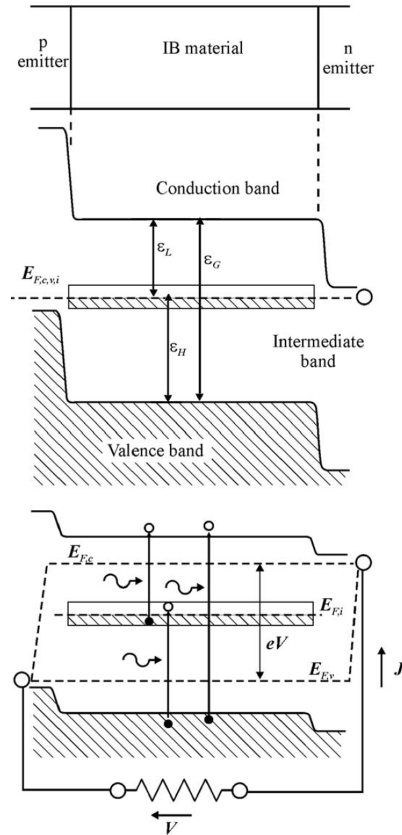

Figure 2.6: *Basic structure of an intermediate band solar cell (top), energy diagram at equilibrium (middle) and energy diagram under forward bias (bottom). Notice the three different excitation paths across ε_L, ε_H and ε_G. The figure is taken from [10] and slightly modified.*

This shows that the energy states for a particle in the quantum dot are discretely quantized. The equation for the energy states also shows that when the dimensions of the quantum dot are decreased, the energy levels of the confined particle actually increase. The magnitude of the energy states can be controlled with a high degree of precision by varying the size of the quantum dot.

Real world quantum dots manufactured by using nanoparticles will have more complex shapes and a finite potential outside the quantum dot, as opposed to an idealised shape and an infinite potential outside as assumed above. A shape that is not perfectly spheric, cylindric or cubic makes the calculations a lot more complex. Also, when the potential outside is finite, the boundary values of the wave function is no longer zero at the edges and the calculations for the wave function inside the well complicates even more.

Still the cubic quantum dot can serve as an approximation and a simplified example to show the basic principles that also apply to the real quantum dot.

2.4.1 Quantum dot growth

The contents of this subsection is taken from [13].

In heteroepitaxy (i.e. the epitaxial growth of films on substrates where the film material is different from the substrate material) typically one of two growth modes are observed.

- *Frank-van der Merwe (layer) growth:* Here epitaxial 2D layer growth is observed. This can be explained due to the atoms or molecules being more strongly bound to the substrate than to each others.

- *Vomer-Weber (island) growth:* Here 3D island growth is observed. This can be explained due to the atoms or molecules being more strongly bound to each others than to the surface.

In addition, when the lattice constants of the film and the substrate are mismatched, a third growth mode may be observed. This growth mode is called the *Stranski-Krastanov growth mode*. Due to the lattice mismatch, a combination of the island and the layer growth modes is seen. For the first few layers an epitaxial film growth is seen, and the film lattice is strained to match the substrate lattice. Then, as the substrate is covered, the top layers will relax into the original lattice constant of the deposited thin film. This leads to islands being formed on top of the epitaxial film, as shown in figure 2.7.

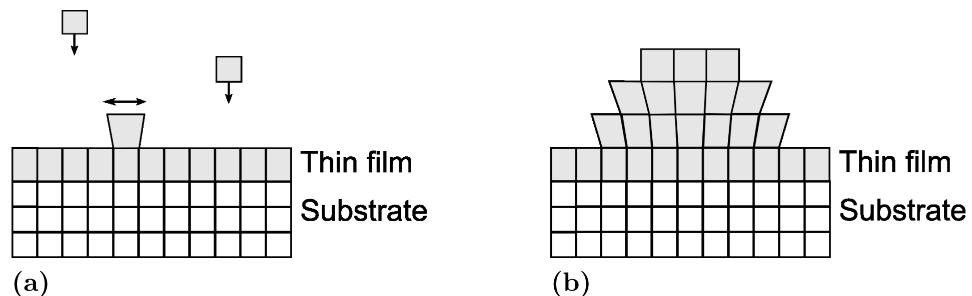

Figure 2.7: *A schematic illustration of the Stranski-Krastanov growth. This illustration shows how the strain due to the lattice mismatch makes island formation more favourable than full film growth after an initial epitaxial layer growth. Based on an illustration in [13].*

InAs has a 7% larger lattice constant than GaAs. Therefore, the Stranski-Krastanov growth mode can be used to grow InAs quantum dots on a GaAs substrate.

2.5 Quantum dot intermediate band solar cells

A quantum dot is sometimes referred to as an *artificial atom*, as the energy states confined in a quantum dot can be compared to the energy states in real atoms. When quantum dots are arranged in a 3D lattice, this can be thought of as a *superlattice* of artifical atoms. A superlattice is a periodic structure with a periodic potential (see chapter 3.5 of [13]). From the periodic potential wells of the quantum dots in the 3D lattice a new energy band arises [10]. This behaviour can be used to create the intermediate band of the intermediate band solar cell [3].

One possible design of a quantum dot intermediate band solar cell is shown in the upper part of figure 2.8. The confined states in the closely spaced quantum dots form the intermediate band in the band gap between the valence band and the conduction band. Electrons can then be pumped by optical excitation from the valence band to the intermediate band, and from the intermediate band to the conduction band. This means that there have to be both filled and empty states in the intermediate band, implying that the Fermi level has to cross it [10].

A number of design constraints for the quantum dot intermediate band solar cell have been identified in [4].

- *Dot size:* The energy states of the quantum dot depend on the shape and size of the dot. For idealized spherical dots made of $In_{0.58}Ga_{0.42}As$ embedded in $Al_{0.4}Ga_{0.8}As$ it has been calculated that the size needs to be in the range of 39 Å. This estimate is not directly related to InAs/GaAs quantum dots, but may give an idea of the typical size order for quantum dots used in intermediate band solar cells.

- *Dot spacing:* The dots should have an as high as possible density in order to provide an as high as possible absorption coefficient without making the bandwidth so large that stimulated emission becomes possible. It has been found that the dots can be stacked together at a distance of 100 Å and that the density of dots can be kept below one order of magnitude from the density of states in the conduction and valence bands without making stimulated emission possible.

- *Dot regularity:* The dot size and spacing of the quantum dot should have a high regularity in order to minimize the bandwidth of the intermediate band. The dispersion in size should preferably be less than 10%.

- *Other factors:* A number of other factors, including the choice of materials, also play an important role in the design of the quantum dot intermediate band solar cell.

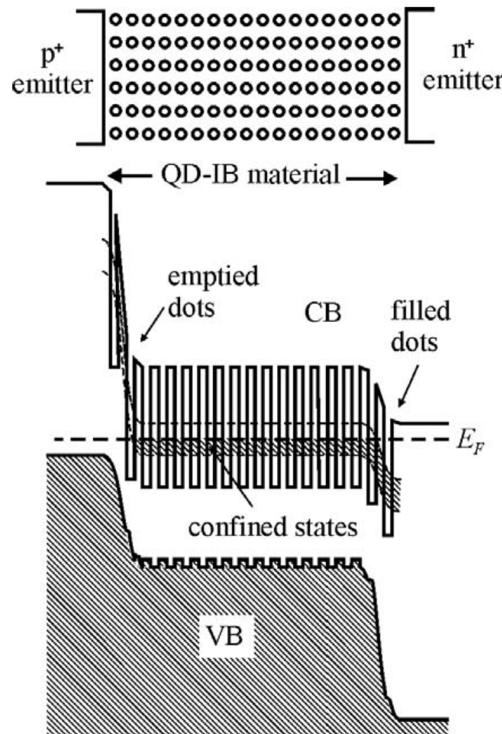

Figure 2.8: *An illustration of the intermediate band formation in a QD-IBSC [10]. On top, an overview of the quantum dot material is seen. Below it, the energy band diagram in equilibrium is shown.*

2.6 Crystal lattices

The theory in this section is taken mostly from [14].

A mathematical concept called a *lattice* is used to describe crystals. A lattice is an infinite grid onto which the *basis* of the crystal is attached. The

basis is a set of one or more atoms that is repeated throughout the lattice, as shown in figure 2.9.

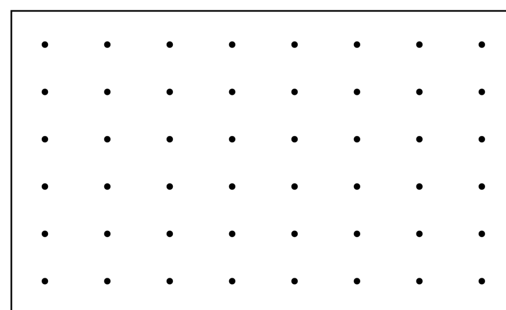

(a)

(b)

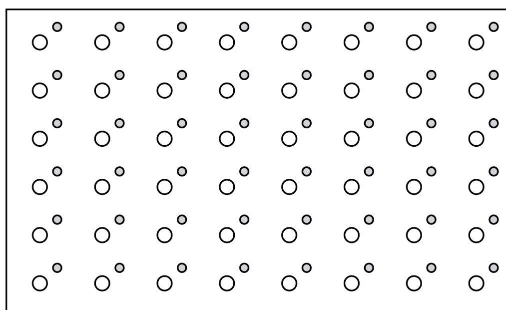

(c)

Figure 2.9: *(a) A two-dimensional lattice. (b) A basis consisting of two atoms. (c) The basis is placed in the lattice. This figure is based on figure 1.2 in [14].*

For any point in a lattice there is an infinite number of similar points. In a three-dimensional lattice, the shortest distance between two identical points along the x axis can be described using a lattice vector called $\mathbf{a}_1$. Likewise, the shortest translation between two points along the y and z axes can be called $\mathbf{a}_2$ and $\mathbf{a}_3$, correspondingly. These vectors are called the *primitive translation vectors* of the crystal. The space bound by these vector is called the *primitive cell*, as shown in figure 2.10. Sometimes a lattice is divided in *unit cells* that are non-primitive for convenience, which are then called *conventional cells.*

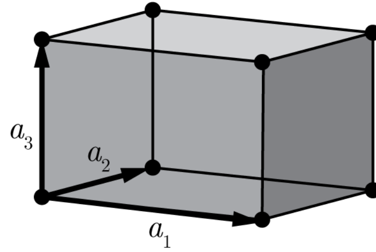

Figure 2.10: *A unit cell with its associated lattice points and its unit vectors* $\mathbf{a}_1$*,* $\mathbf{a}_2$ *and* $\mathbf{a}_3$*. This figure is based on figure 1.3b in [14].*

Simple cubic structure

The simple cubic structure is a type of lattice structure where the three primitive translation vectors are of identical length and perpendicular to each others. Then they are given as $\mathbf{a}_1 = a\hat{\mathbf{x}}$, $\mathbf{a}_2 = a\hat{\mathbf{y}}$ and $\mathbf{a}_3 = a\hat{\mathbf{z}}$ where a is the length of one of the sides of the primitive cell, also called the *lattice constant*. The lattice constant varies depending on the element(s) used, the temperature and the stresses present in the lattice.

The primitive cell in this lattice is cubic with an atom in each corner, as shown in figure 2.11.

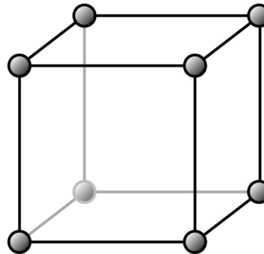

Figure 2.11: *The primitive cell of a simple cubic lattice.*

Face centered cubic structure

In the face centered cubic (fcc) structure, the unit vectors are given as $\mathbf{a}_1 = \frac{1}{2}a(\hat{\mathbf{x}}+\hat{\mathbf{y}})$, $\mathbf{a}_2 = \frac{1}{2}a(\hat{\mathbf{y}}+\hat{\mathbf{z}})$ and $\mathbf{a}_3 = \frac{1}{2}a(\hat{\mathbf{z}}+\hat{\mathbf{x}})$. The angle between the vectors is 60°.

Figure 2.12 shows both the conventional and the primitive cell of the face centered cubic structure.

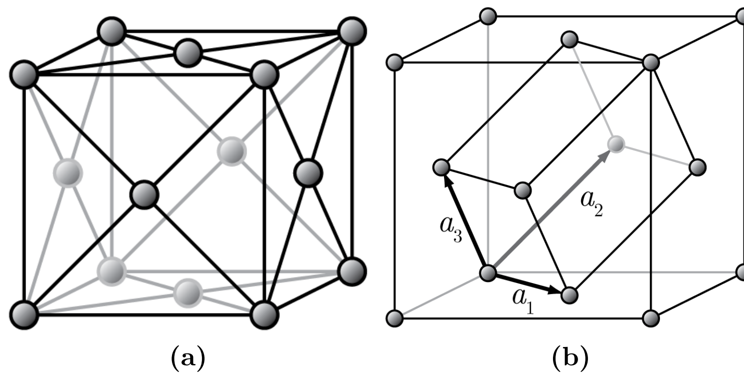

Figure 2.12: *(a) A conventional cell of the fcc structure. (b) A primitive cell of the fcc structure. This figure is based on figures 1.8 and 1.11 in [14].*

Zinc blende structure

The zinc blende structure is identical to the face centered cubic lattice, but has a basis consisting of two atoms of different elements. The coordinates of the two atoms in the basis is $(0, 0, 0)$ and $(\frac{1}{4}a, \frac{1}{4}a, \frac{1}{4}a)$ with a being the lattice constant. Examples of solids with the zinc blende structure are gallium arsenide and indium arsenide. The zinc blende structure is shown in figure 2.13.

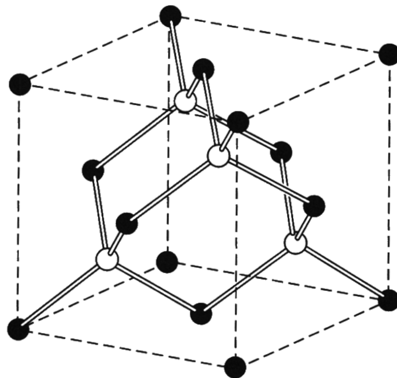

Figure 2.13: *A conventional cell of the zinc blende structure. This figure is taken from figure 1.24 in [14].*

2.6.1 Crystal planes

Planes in a crystal is described using a (hkl) notation where h, k and l are found using the following procedure:

- Find the intercepts on the axes in terms of the lattice constants $\mathbf{a}_1$, $\mathbf{a}_2$ and $\mathbf{a}_3$.
- Take the reciprocal of these numbers and reduce them to three integers having the same ratio.

An example of a plane is shown in figure 2.14.

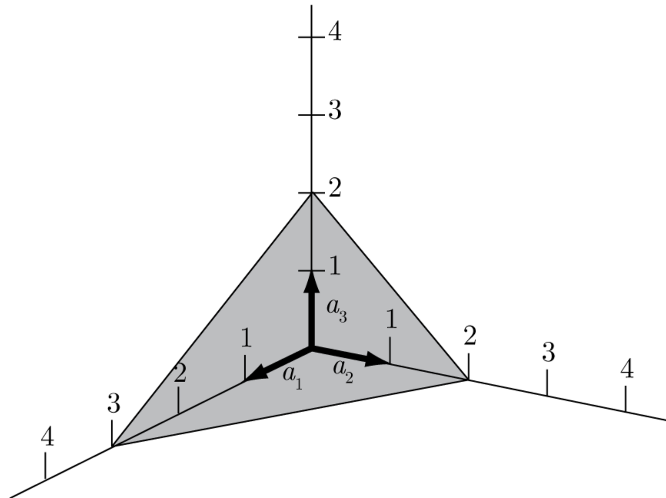

Figure 2.14: *The plane in the figure intercepts the axes at 3, 2, 2. The reciprocals of these intercepts are* 1/3, 1/2 *and* 1/2*, meaning the plane has indices* (233)*. This figure is based on figure 1.13 in [14].*

When a plane cuts through the negative side of an axis, this is denoted by placing a minus sign over the index, like this: $(h\bar{k}l)$.

In cubic crystal systems, the $[hkl]$ notation describes a direction that is perpendicular to the (hkl) plane.

2.6.2 Monolayers

A monolayer is a single layer of atoms or molecules. For the simple cubic lattice, every translation along the primitive lattice vectors equals one monolayer, as only one monolayer of atoms needs to be added to the lattice to create another layer of unit cells.

However, for the face cubic lattice two monolayers of two-atom molecules needs to be added to add another layer of conventional unit cells to the lattice (one layer for the face centred atoms, and one layer for the atoms at the corners). This means that in order to grow a layer of a face centred lattice that has the thickness of one lattice constant, two monolayers of atoms or

molecules must be grown. This also applies to the zinc blende structure, as it is a face centred lattice with two-atom molecules.

2.6.3 Strain

When a crystal is deposited on top of another crystal with a different lattice constant, this leads to the crystal being strained. The in-plane strain is defined as[15]:

$$e_{xx} = \frac{a_x - a_0}{a_0}$$

where a_0 is the lattice constant of the lattice that is being grown and a_x is the lattice constant of the other crystal that it is grown on top of.

And the strain in the growth direction is given as:

$$e_{zz} = \frac{-2C_{12}}{C_{11}} e_{xx}$$

where C_{11} and C_{12} are elastic moduli taken from the stiffness tensor of the material.

Then the lattice constant in the z direction can be calculated as follows:

$$a_z = a_0(1 + e_{zz})$$

For instance, when InAs, which has a lattice constant of 0.60591 nm at 26° Celsius and elastic moduli $C_{11} = 83.29$ and $C_{12} = 45.26$ is grown on top of GaAs which has a lattice constant of 0.56532 nm at 26° Celsius, the lattice constant in the z direction for InAs becomes 0.65002 nm under strain.

2.7 X-ray diffraction

The theory in this subsection is taken mostly from [7] and [14].

2.7.1 Plane waves

A wave that propagates along a one dimensional line, or a *plane wave*, can be described using the periodic cosine function: $y(x, t) = A\cos(\omega t - kx + \phi)$ where A is the amplitude, ω is the angular frequency, k is the wave number and ϕ is the phase of the wave, as shown in figure 2.15.

The angular frequency can also be written as $\omega = 2\pi f = 2\pi/T$ where f is the frequency and T is the period of the wave, as shown in figure 2.15. The wave number is given as $k = 2\pi/\lambda$ where λ is the wavelength of the wave.

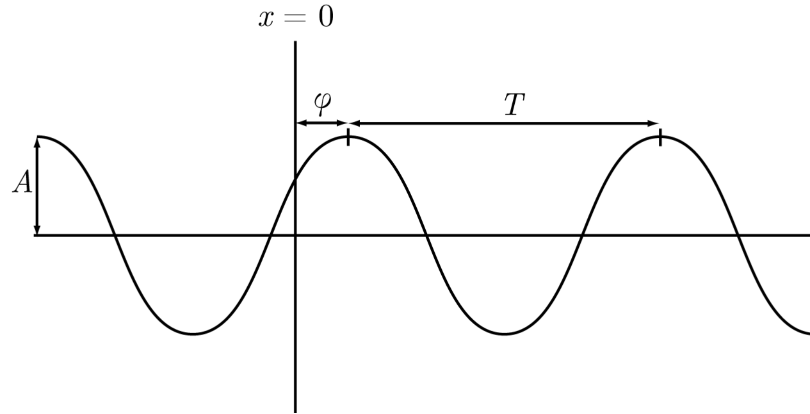

Figure 2.15: *The amplitude A, the period T and the phase ϕ of a wave. The phase of a cosine wave is the difference between the y axis and the nearest peak of the wave.*

Given two synchronous waves $y_1(x,t)$ and $y_2(x,t)$ (i.e. having the same amplitude, frequency and phase) that meet at the same point after having travelled two different paths to the point. The two waves can be written as:

$$y_1 = A\cos(kx_1 - \omega t + \phi)$$

$$y_2 = A\cos(kx_2 - \omega t + \phi)$$

where $(x_2 - x_1)$ is the different in path length between the two waves.

The wave observed at this point will then be the superposition of the two waves: $y = y_1 + y_2$. By using the trigonometric identity $\cos\alpha + \cos\beta = 2\cos[(\alpha+\beta)/2]\cos[(\alpha-\beta)/2]$ the sum can be written as:

$$y = 2A\cos\left[\frac{k(x_1+x_2)}{2} - \omega t + \phi\right]\cos\left[\frac{k(x_1-x_2)}{2}\right]$$

There are two special cases of the superposition of these two waves. First, if $k(x_2 - x_1)/2 = n\pi$ where n is any arbitrary integer, then the cosine component of y will be equal to 1 or -1, and the resulting wave will then be a wave with twice the amplitude of the waves y_1 and y_2. This is called *constructive interference*, as shown in figure 2.16. Second, if $k(x_2 - x_1)/2 = ((2n+1)/2)\pi$, then the cosine component will be zero, and the resulting wave will cancel. This is called *destructive interference*, as shown in figure 2.17.

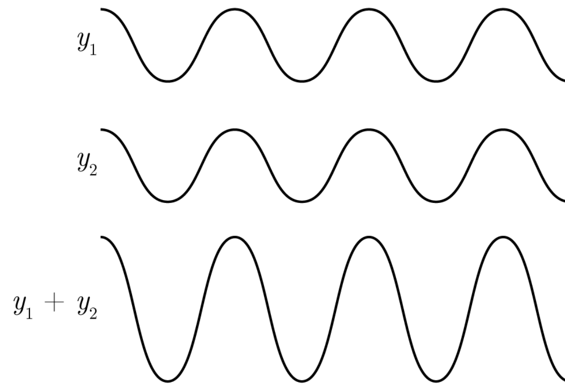

Figure 2.16: *The constructive interference of two waves y_1 and y_2*

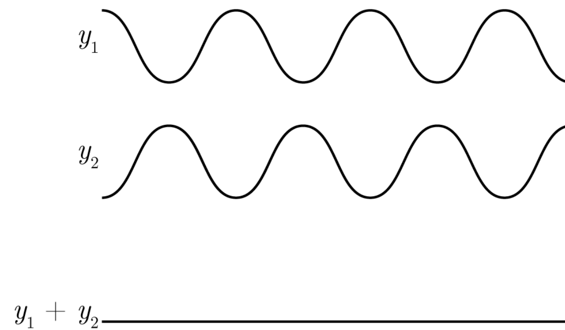

Figure 2.17: *The destructive interference of two waves y_1 and y_2*

Beat

Beat occurs when two waves with frequencies that are very close, but not identical, are added. Mathematically it can be explained as follows:

$$\sin(2\pi f_1 t) + \sin(2\pi f_2 t) = 2\cos(2\pi \frac{f_1 - f_2}{2} t)\sin(2\pi \frac{f_1 + f_2}{2} t)$$

The frequency of the resulting wave is the average of the frequencies of the original waves, with an envelope with frequency equal to half the difference of the original wave frequencies, as shown in figure 2.18. The resulting wave appears to vary in amplitude.

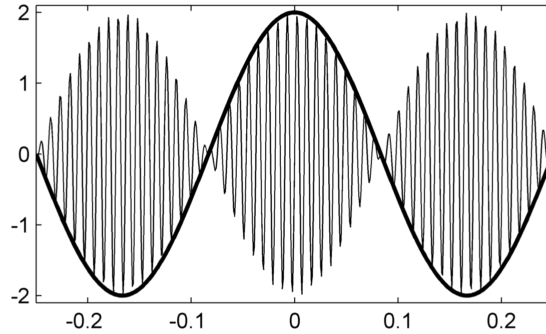

Figure 2.18: *A superposition of two waves with frequencies 104 Hz and 110 Hz, and the enveloping cosine wave. Note that the wave undergoes a 180° phase shift every time the cosine function crosses zero.*

2.7.2 Bragg's law

In figure 2.19 parallel atomic planes are shown which function as plane reflectors. The distance between these parallel planes is d. The angle between the incident beam and the normal to the planes (θ) is equal to the angle between the normal and the reflected beam.

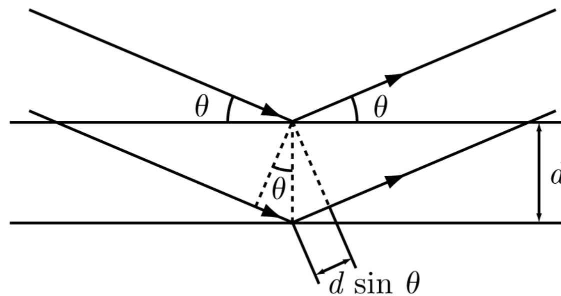

Figure 2.19: *Two parallel waves are shown reflecting from two parallel atomic planes separated by the distance d. This figure is based on figure 2.2 in [14].*

As shown in figure 2.19, the path difference between the two neighbouring waves can be written as $\Delta = 2d\sin\theta$. When the path difference is equal to an integer multiple of the wave length λ, the waves will reinforce each others. This is called a Bragg reflection, and occurs at any integer multiple of λ:

$$2d\sin\theta_B = n\lambda$$

This equation is called Bragg's law. If the path difference is equal to half the wavelength (or to any integer multiple of the wavelength plus a half) the reflected waves will cancel each other: $2d\sin\theta = (n+1/2)\lambda$

The Bragg angle θ_B is determined by the spacing of the reflection planes. For a given crystal plane (hkl) in the unit cell of a crystal with lattice constant a, the interplanar spacing is:

$$d = \frac{a}{\sqrt{h^2 + k^2 + l^2}}$$

2.7.3 X-rays and x-ray diffraction

X-rays is electromagnetic radiation with wavelengths in the range of approximately 0.01 to 1 nanometers.

X-rays are produced when high-energy electrons are slowed down and lose energy. This can be done by applying a high voltage (at the magnitude of 10 kV) between a cathode and an anode. Then high-energy electrons are drawn out of the cathode and collide with the anode. When this happens, x-rays are emitted. The highest energy electrons will have the frequency defined as $q_e V = hf_{max}$, where $q_e = 1.60218 \times 10^{-19}$C is the fundamental charge of electrons and V is the voltage applied between the electrodes. The shortest wavelength of the x-ray photons emitted is $\lambda_{SWL} = hc/q_e V$.

Crystal structures can be studied through the diffraction of waves. When the wavelength is of roughly the same magnitude as the lattice constant (which is the case for x-rays in crystalline solids) the diffracted beams will carry information about the crystal structure, as shown by Bragg's law. These beams will show clear peaks in intensity when constructive diffraction is present, which can be used to determine the periodicity of the crystal lattice by using Bragg's law.

2.7.4 Superlattices

The theory in this subsection is taken from subsection 4.7.3 in [16].

A superlattice is a structure with another periodicity additional to the lattice periodicity. One example is a *heterostructure* (a structure consisting of two different semiconductor materials) consisting of two different materials A, B ordered on top of each other (ABABAB...) as illustrated in figure 2.20. The period D is the sum of the thickness of the A and B layers $D = D_A + D_B$. The superlattice creates an extra periodicity in the lattice that leads to a extra diffraction pattern superimposed on the diffraction pattern due to the normal lattice periodicity, provided that the wavelength of the x-rays is roughly comparable to the period of the superlattice.

The superlattice peaks will then be at angles θ such that $2D \sin\theta = L\lambda$ where L is an integer. Since the superlattice is in the z direction, the $hk0$

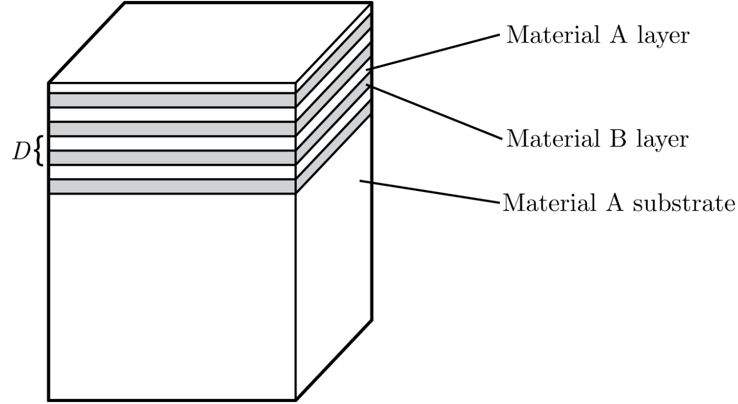

Figure 2.20: *Schematic illustration of a superlattice. It consists of two materials A and B stacked alternately. D is the thickness of one superlattice period. This figure is based on figure 4.15 in [16].*

reflections are unaffected by the superlattice effect while the $00l$ reflections are strongly affected.

If A and B are two binary zinc blende materials, then the thickness of the layers A and B are:

$$D_A = \frac{n_A a_A}{2}$$
$$D_B = \frac{n_B a_B}{2}$$

where n_A and n_B are the number of monolayers and a_A and a_B are the lattice constant of A and B, respectively.

Then $D = (1/2)(n_A a_A + n_B a_B)$, and Bragg reflection occurs at angles:

$$\sin\theta = \frac{L\lambda}{n_A a_A + n_B a_B}$$

When $L = (l/2)(n_A + n_B)$ with l as an integer,

$$\sin\theta = \frac{(n_A + n_B)l\lambda}{2(n_A a_A + n_B a_B)} = \frac{l\lambda}{2\langle a\rangle}$$

which reduces to the Bragg formula for scattering from a crystal lattice with lattice constant $\langle a\rangle$, the average lattice constant of the superlattice. This superlattice diffraction peak is called the *zero-order* peak and will be somewhere between the Bragg peak of material A and the Bragg peak of material B. The other reflection peaks of the superlattice are called *satellites*, with indicies -2, -1, $+1$, $+2$, etc. An x-ray diffraction pattern from a GaAs/AlAs superlattice is shown in figure 2.21.

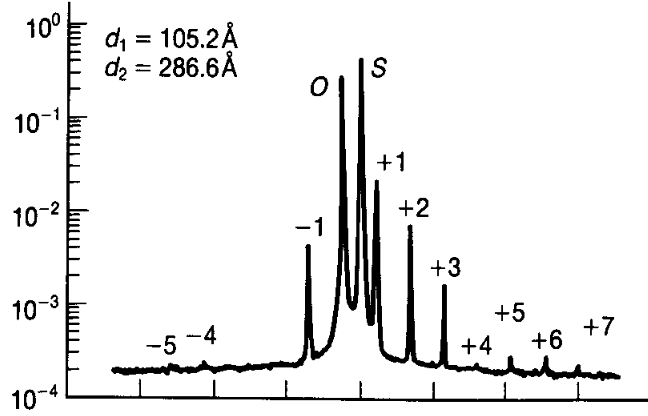

Figure 2.21: *X-ray diffraction spectrum from a GaAs/AlAs superlattice. S is the substrate peak, O is the zero-order superlattice peak and the other superlattice peaks are numbered +3, +2, +1, −1 etc. This figure is taken from figure 4.16 in [16].*

The Bragg equation can be written as $2D\sin(\theta_p + \theta_B) = m\lambda$ where θ_p is the angular separation between a superlattice peak of order p and the zero-order superlattice peak, θ_B is the zero-order peak as described above and m is an integer. Then, for two superlattice orders p, q:

$$2D\left[\sin(\theta_p + \theta_B) - \sin(\theta_q + \theta_B)\right] = (p-q)\lambda$$

Since θ_p and θ_q are small, $\sin\theta_{p,q} \approx \theta_{p,q}$ and $\cos\theta_{p,q} \approx 1$. Then, by using the trigonometic identity:

$$\sin(\alpha + \beta) = \sin\alpha\cos\beta + \sin\beta\cos\alpha$$

the equation above can be rewritten to:

$$2D(\theta_p\cos\theta_B - \theta_q\cos\theta_B) = (p-q)\lambda$$

so that

$$D = \frac{(p-q)\lambda}{2\Delta\theta_{p,q}\cos\theta_B}$$

where $\Delta\theta_{p,q} = \theta_p - \theta_q$ is the angular separation of two satellites p and q.

Chapter 3

Experimental methodology

3.1 Molecular beam epitaxy

Molecular beam epitaxy (MBE) is a method of depositing a crystalline film (called an *epilayer*) on a crystalline substrate. A schematic drawing of an MBE growth chamber is shown in figure 3.1.

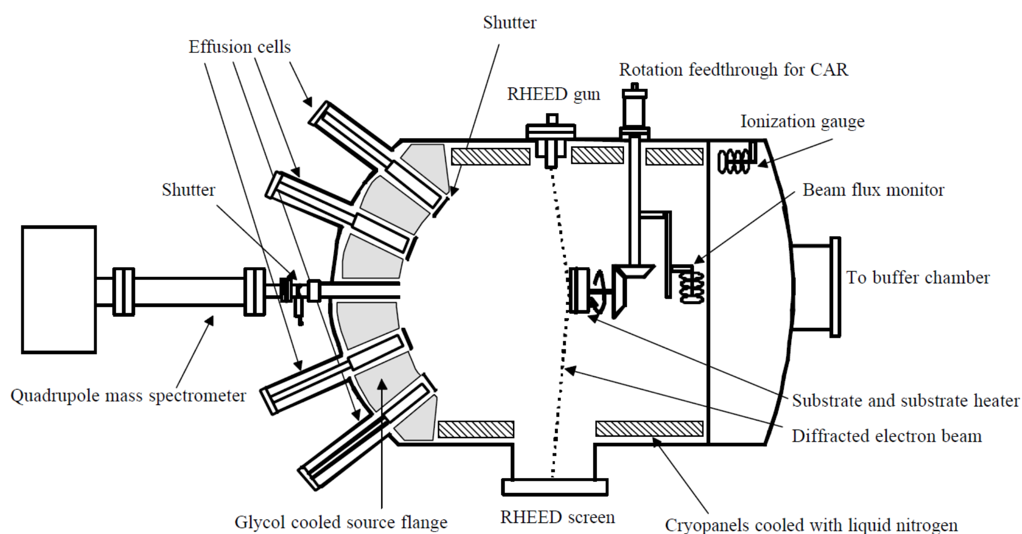

Figure 3.1: *A schematic drawing of the MBE growth chamber [15].*

Ultra-pure elements are heated in separate effusion cells until they slowly sublimate. The resulting gas then flows as a molecular beam into the main chamber where the sample is situated. When the beams reach the sample

substrate, they condense on the surface if the temperature is appropriate. In this way, a crystalline solid is built up layer by layer. The MBE growth process can be controlled with an atomic resolution of thickness. This process happens under ultra high vacuum to ensure a high purity of the grown material (see chapter 8 in [12] and chapter 11 in [17]).

A number of growth parameters can be varied in the molecular beam epitaxy growth process. The shutters of the effusion cells can be opened and closed individually to allow or stop the gas flowing from the effusion chamber into the main chamber. Also, the flux of the gases from the effusion cells can be controlled by varying the temperature inside the effusion cells. In the main chamber, the temperature of the substrate (also called the *growth temperature*) can be controlled using a substrate heater. The film growth is monitored using an *reflection high-energy electron diffraction* (RHEED) system. An electron gun emits a high energy electron beam. This beam is diffracted and reflected from the sample onto a fluorescent screen. By monitoring the time variation of the diffraction pattern that is seen on this screen, the film thickness and growth speed can be determined.

The positioning and contents of the effusion cells relative to the sample is illustrated in figure 3.2. The angle between individual effusion cells is 45°. Also the angle between the sample plane and the effusion cells is 57°, as illustrated in figure 3.3.

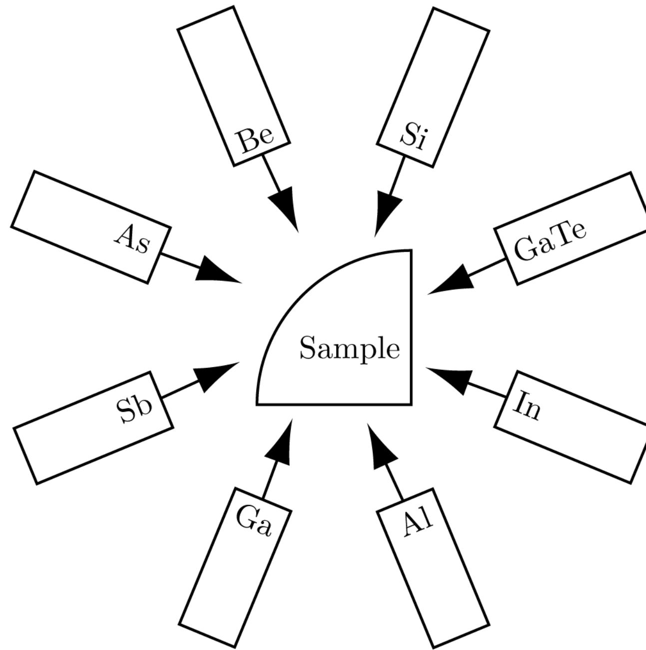

Figure 3.2: *The effusion cells in the MBE growth chamber.*

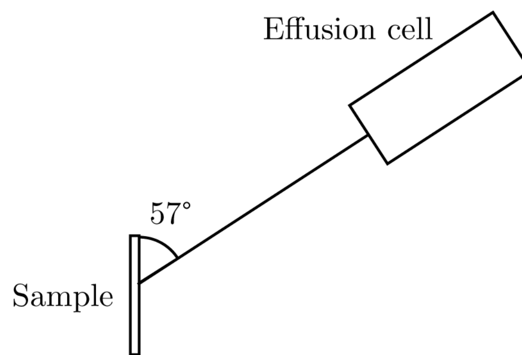

Figure 3.3: *The positioning of an effusion cell relative to the sample, seen from the side.*

3.1.1 Deposition thickness as a function of the location on the sample

When a sample is not rotated during MBE deposition, the deposition thickness across the sample will vary depending on the distance from the source.

Figure 3.4 shows a single MBE effusion cell and the plane that the sample lies in, seen from the front and from the side. In this figure r is the distance from the source to the sample, n is a line that is normal to the sample plane, and l is the distance between the end points of n and r on the sample plane. These three lines together create a right-angled triangle. r_0 and l_0 are the corresponding values for r and l when r ends at the origin in the sample plane. The angle between r_0 and l_0 is 57°. When choosing an r different from r_0, l becomes equal to $\sqrt{x^2 + (l_0 + y)^2}$, where x and y denote the displacement from the origin in the sample plane.

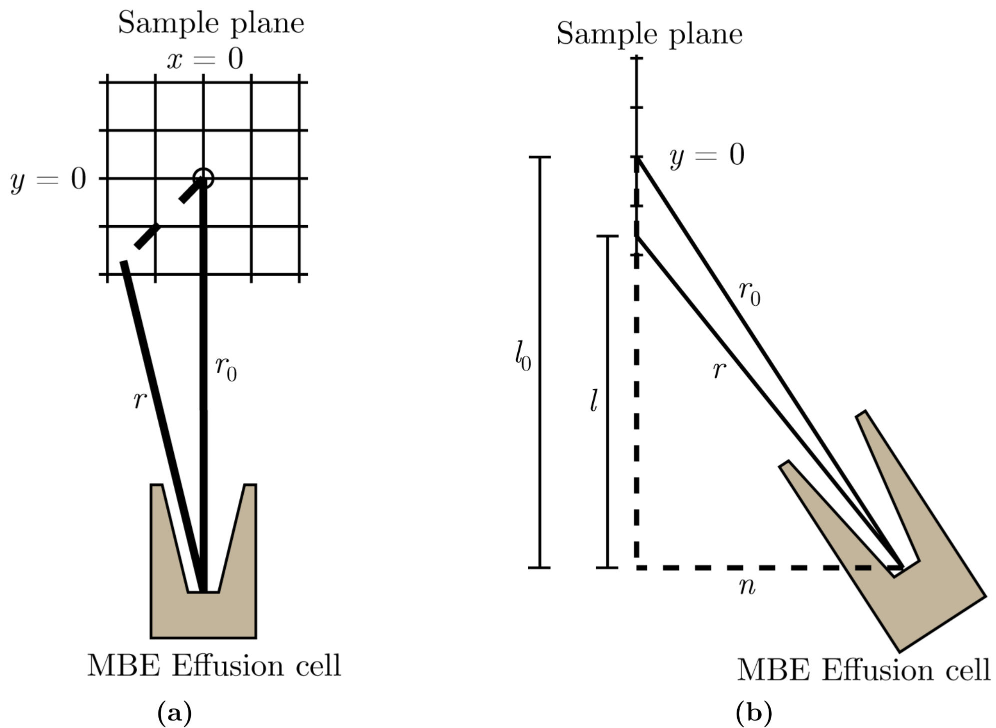

Figure 3.4: *(a) The MBE effusion cell and the sample plane, seen from the front. (b) The MBE effusion cell and the sample plane, seen from the side. In both figures the sample plane is oriented relative to the MBE effusion cell.*

This leads to the following equations:

$$n^2 + {l_0}^2 = {r_0}^2$$

$$n^2 + l^2 = n^2 + x^2 + (l_0 + y)^2 = (r_0 + \Delta r)^2$$

where Δr is the change in r from r_0 caused by the x and y translation in the sample plane.

Equating the n in both equations, expanding the parentheses and ordering the equation yields:

$$(\Delta r)^2 + 2r_0\Delta r - (x^2 + 2l_0 y + y^2) = 0$$

This is now a quadratic equation in Δr. Solving the equation leads to:

$$\Delta r = -r_0 \pm ({r_0}^2 + 2l_0 y + x^2 + y^2)^{1/2}$$

The negative root would be at the magnitude of $-2r_0$ when x and y are small relatively to r_0. This would lead to a negative r. That is unreasonable and the negative root is discarded.

As mentioned earlier, the angle between r_0 and l_0 is 57°. Then $\cos 57° = l_0/r_0$. This can be inserted in the positive root of Δr, which then becomes:

$$\Delta r = ({r_0}^2 + x^2 + y^2 + 2yr_0 \cos 57°)^{1/2} - r_0$$

The flux at a distance r from the source can be written as $F = b/r^2$ where b is a constant.

Then the flux density at any given point of the sample plane can then be found by inserting the equation for r into F:

$$F_{x,y} = b\frac{1}{(r_0 + \Delta r)^2} = b\frac{1}{(r_0 + ({r_0}^2 + x^2 + y^2 + 2yr_0 \cos 57°)^{1/2} - r_0)^2}$$
$$= b\frac{1}{{r_0}^2 + x^2 + y^2 + 2yr_0 \cos 57°}$$

At the origin of the sample plane the flux density is: $F_{0,0} = b/{r_0}^2$. Then the change of flux density at any point on the sample surface plane relative to the flux density at the origin is:

$$\frac{F_{x,y}}{F_{0,0}} = \frac{{r_0}^2}{{r_0}^2 + x^2 + y^2 + 2yr_0 \cos 57°}$$

3.2 X-ray diffraction

A *rocking curve scan* is a x-ray scan where the x-ray diffraction angle is limited to a small area around the strongest Bragg peak of the sample substrate. As shown in figure 3.5, the angle ω between the incident wave and the sample is varied while the angle 2θ between the incident and the outgoing wave is constant.

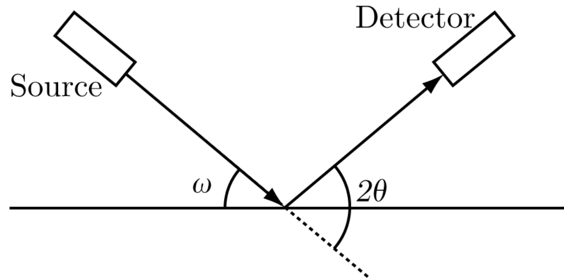

Figure 3.5: *Set-up for x-ray rocking curve scan.*

In this thesis the 004 reflection is being studied with an x-ray wavelength of 0.15406 nm. The Bragg law can be used to estimate the Bragg reflection angle for GaAs and InAs. For the 004 reflection the difference in path length for two neighbouring reflected waves is 4λ, and therefore $n = 4$ in the Bragg equation. For the zinc-blende lattice the interplanar spacing is $d = a$ with a being the lattice constant of the conventional unit cell. Then the Bragg equation simplifies to:

$$\sin\theta_B = \frac{2\lambda}{a}$$

The lattice constants for GaAs and InAs are 0.56532 nm and 0.60591 nm at 26° Celsius, respectively[15]. Using these lattice constants, the strongest Bragg reflection angles can be calculated to be:

$$\theta_{\mathrm{B(GaAs)}} = 33.027°$$

$$\theta_{\mathrm{B(InAs)}} = 30.566°$$

The x-ray diffraction setup used is a *D8 Discover* manufactured by Bruker-AXS. The software *XRD Commander* version 2.6.1 was used to control the x-ray equipment and sample holder, *XRD Wizard* version 2.9.0.22 was used to program measurement sequences for experiments and the 2007 version of *EVA* was used to analyse the measurement results (all of these are from

Bruker-AXS). During the rocking curve scans, a circular aperture of 1.0 mm was attached to the x-ray source. With this aperture the x-ray beam is circular and about 1 mm in diameter. 2θ was set to 66.05694° (this value was calculated using XRD Wizard), and ω was varied from 32.7285° to 33.4785° with a step size of 0.001° and a step time of 10 seconds. The x-ray source voltage and current were set to 40 kV and 40 mA, respectively. The x-ray wavelength emitted was 0.15406 nanometers. The numerical computing software *MATLAB* version 7.13.0.564 from MathWorks was used to analyse and plot the measurement results.

Chapter 4

Simulations

In this chapter a number of simulations are presented. In section 4.1 simulations of MBE gas flux are presented. Then simulations of x-ray scans are presented in section 4.2.

4.1 MBE flux simulation

The distribution of In and Ga across the wafer was simulated using the numerical computing software MATLAB version 7.13.0.564 from MathWorks. It is assumed the sample is grown with an abundance of As, meaning the amounts of In and Ga during MBE growth determine the thicknesses of the InAs and GaAs layers on the sample, respectively. Note that in the flux simulations the sample and the sources have been rotated 180° compared to the orientation in figure 3.2.

The results from the simulation for In are shown in figure 4.1. In this simulation the lowest relative flux density is -2.4% on the curved edge near the upper right corner, and the highest relative flux density is 4.4% at the upper left corner. This means the In flux density varies by $\pm 3.4\%$ across the sample.

The results from the simulation for Ga are shown in figure 4.2. In this simulation the lowest relative flux density is -4.4% at the lower left corner, and the highest relative flux density is 4.4% at the upper right corner, which means the Ga flux density varies by $\pm 4.4\%$

The source code for this simulation can be seen in appendix A.1.

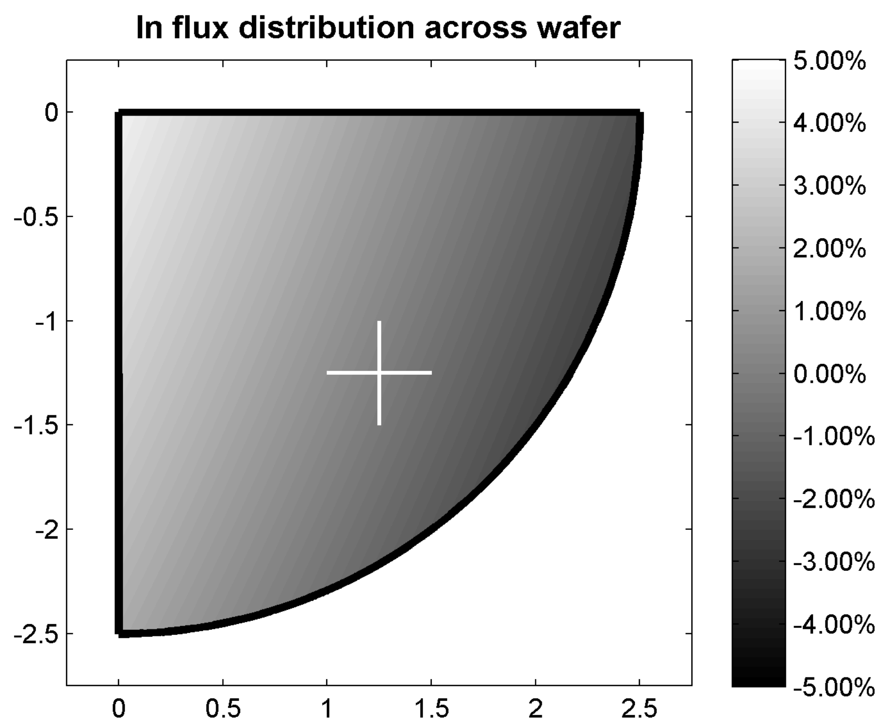

Figure 4.1: *In flux distribution simulation. The origin of the flux simulation is marked with a cross.*

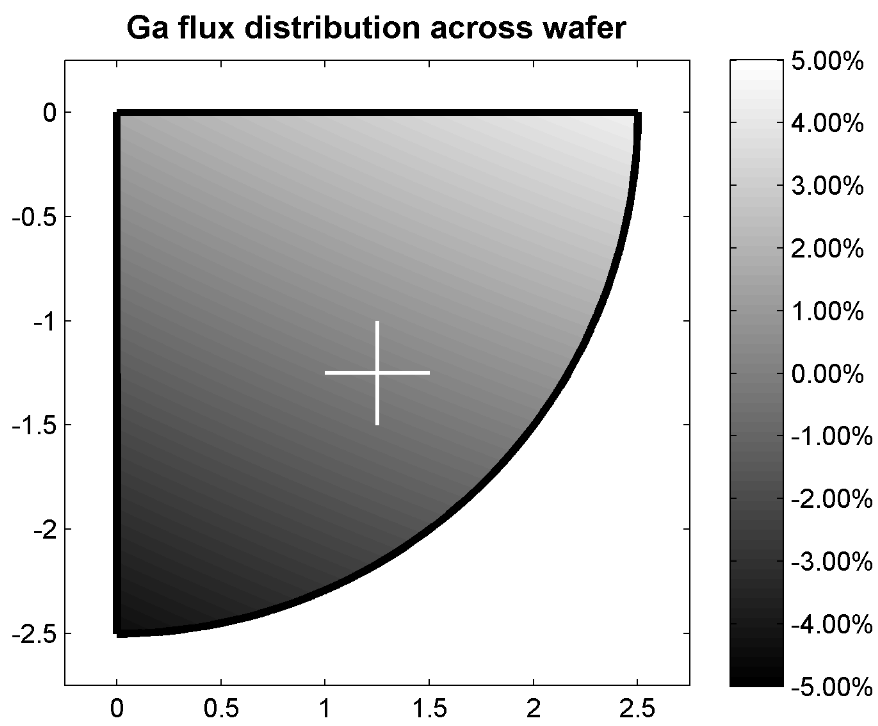

Figure 4.2: *Ga flux distribution simulation. The origin of the flux simulation is marked with a cross.*

4.2 X-ray diffraction simulations

X-ray rocking curve scans were simulated using LEPTOS software, version 2.03 (build 1). In LEPTOS, sample structures are simulated by first choosing a substrate material, then entering the material type and thickness of the various thin film layers on top of it, in the z direction. In case of alloys, the amount of the various elements is also chosen. The crystal is assumed to be infinite in the x and y directions. LEPTOS then calculates an x-ray diffraction pattern based on this input.

In LEPTOS, the x-ray wavelength was set to 0.15406 nm and the simulations were done around the 004 reflection. The RMF (Recursive Matrix Formalism) was set to 4x4, the instrumental function was pseudo-Voigt (meaning both Gaussian and Lorentzian distributions are used for convolution) with the Gaussian dispersion set to 200, the Lorentz factor set to 0.01 and the weight coefficient between the Gaussian and the Lorentzian functions set to 0.3. These are standard values. LEPTOS was set to simulate a rocking curve scan between 31 and 35 degrees with an increment of 0.001 and 2θ equal to 66.05694. This value was calculated in XRD Wizard.

The lattice constant that is used to calculate InAs thicknesses is set to 0.65002 nm to account for strain. This is a good approximation for InAs thicknesses of 0-2 ML. However for 2-4 ML this might be a less good approximation as the InAs lattice becomes relaxed in this range and approaches the relaxed lattice constant at 0.60591 nm.

All simulations are based on a basic structure of a 70 nm GaAs layer sandwiched between two 2 ML InAs layers, all this on top of a GaAs substrate. A schematic drawing of the structure is shown in figure 4.3.

A simulation of this structure is seen in figure 4.4. In this figure a sharp peak from the GaAs substrate and superlattice peaks from the InAs/GaAs structure can be observed.

MATLAB was used for plotting the simulations, and also for estimating the peak locations of the simulations. The algorithm used for estimating peak locations is as follows: The slope in every single point is calculated based on the change from the point before to the point after the given point. If the slope is positive in a point A and zero in the next point B and negative in the next point after that C, it is assumed the peak is at point B (and the uncertainty of the peak location is $\pm 0.001°$ since the step size of the simulation is $0.001°$). If the slope changes from positive in a point A to negative in the next point B, it is assumed the peak is in the middle between points A and B (and the uncertainty of the peak location is $\pm 0.0005°$ since the step size of the simulation is $0.001°$).

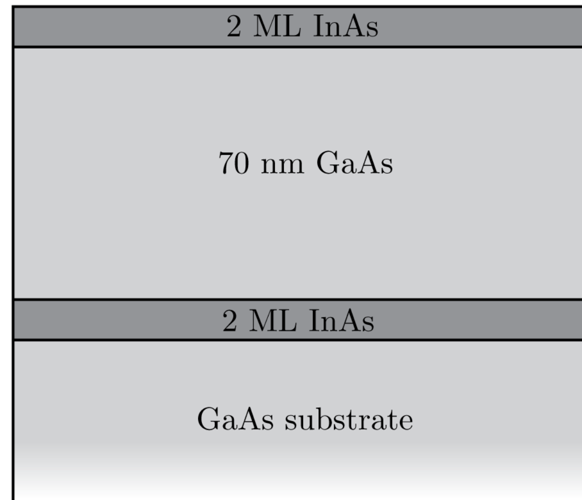

Figure 4.3: *Schematic drawing of the basic structure used in the simulations.*

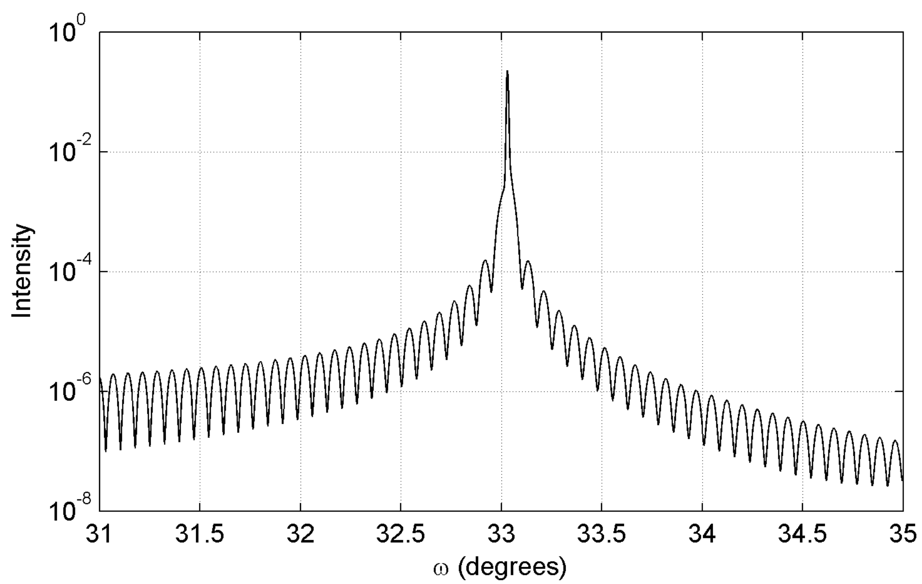

Figure 4.4: *A simulation of the sample seen in figure 4.3.*

4.2.1 GaAs spacer thickness

A set of simulations was made where the thickness of the GaAs spacer layer was varied with 1 nm steps from 60 nm to 80 nm. The thicknesses of the other layers were kept constant.

Parts of the results are shown in figure 4.5. In this figure, it can be seen that the angular separation of the superlattice peaks decreases as the thickness of the GaAs layer increases. Two superlattice peaks can be seen between 33.1 and 33.3 degrees at 60 nm in the figure, while three peaks can be seen in the same interval at 80 nm.

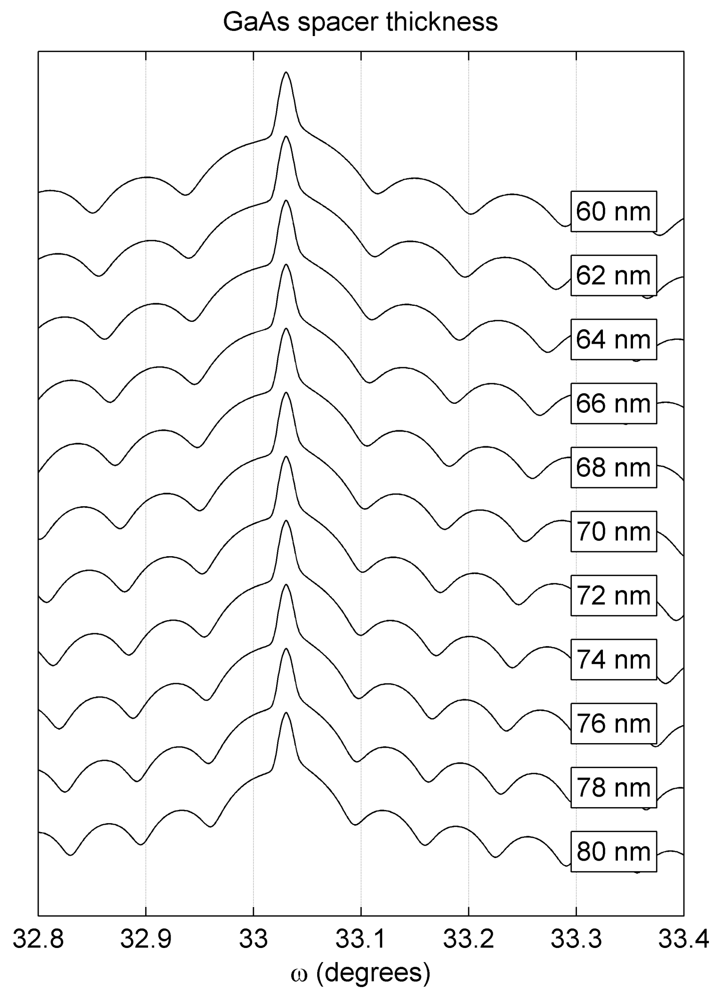

Figure 4.5: *Parts of the simulations with varying GaAs spacer thickness.*

The exact position of the zero-order peak can not be found as it is hidden by the GaAs Bragg peak. The location of this peak was estimated by finding the average of the location of the -2 and +2 peaks. The results are shown in figure 4.6. From this figure it can be seen that the estimated position of the zero-order peak increases as the GaAs thickness increases. The difference between the position at 60 nm and the position at 80 nm is 0.012°. This change can be explained as follows: when the amount of GaAs in the superlattice is increased, the average lattice constant decreases and the zero-order peak shifts closer to the Bragg peak from the GaAs substrate.

The superlattice thickness was calculated based on the superlattice peaks as follows: First a plot is made with the $2\sin(\omega)/\lambda$ of every peak on the y axis and the order of the peaks on the x axis, as shown in figure 4.7 for the simulation with 70 nm GaAs layer. Then a straight line is fitted to this plot. The superlattice thickness is then the inverse of the slope of this line.

The superlattice thicknesses has been estimated for all simulations, and the results are presented in table 4.1 and figure 4.8. From the figure it can be seen that the superlattice thickness seems to increases linearly as the GaAs spacer thickness increases.

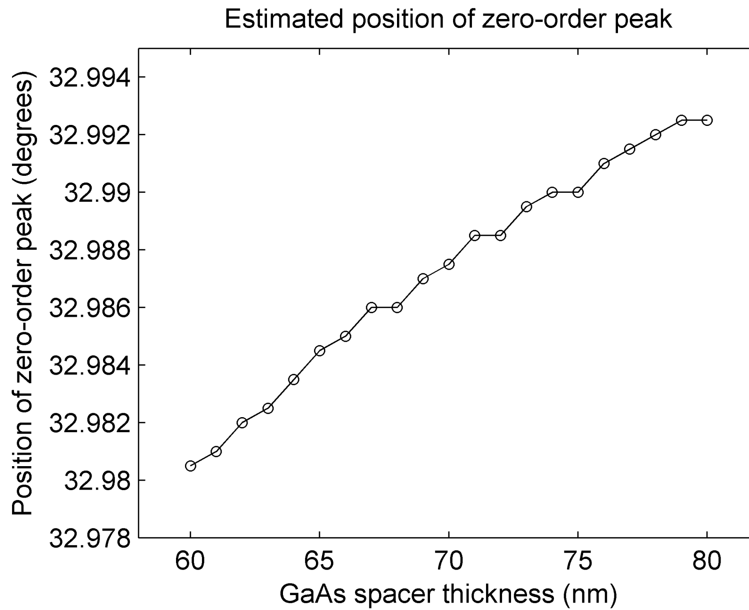

Figure 4.6: *Change in the estimated zero-peak position as the thickness of the GaAs buffer layer increases.*

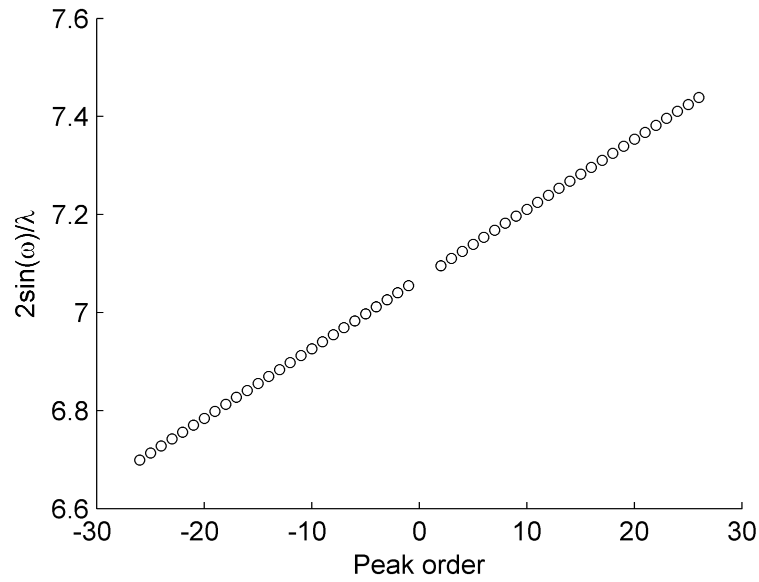

Figure 4.7: *The order and the* $2\sin(\omega)/\lambda$ *for every peak. The gap in the middle of the plot is due to the 0 and 1 peaks being hidden by the GaAs Bragg peak.*

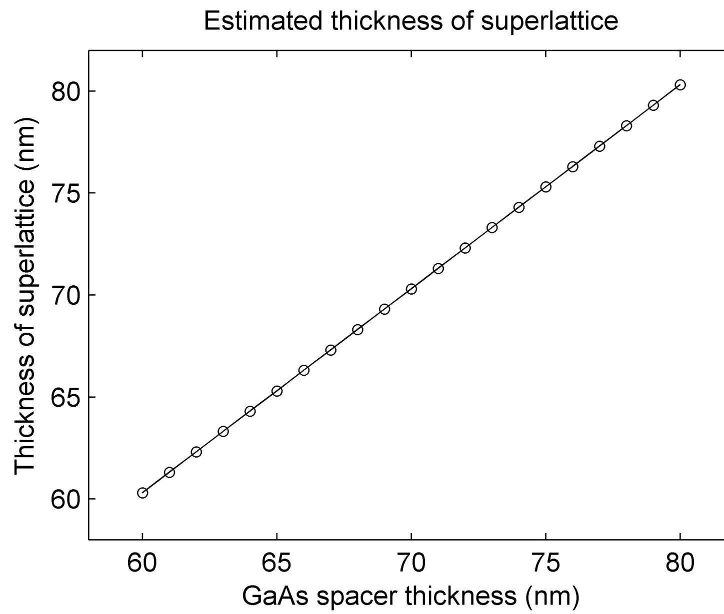

Figure 4.8: *Estimated superlattice thickness as a function of GaAs spacer thickness.*

Table 4.1: *Estimated superlattice thickness as a function of GaAs spacer thickness.*

GaAs thickness	**Estimated superlattice thickness**
60 nm	60.31 nm
61 nm	61.31 nm
62 nm	62.30 nm
63 nm	63.31 nm
64 nm	64.30 nm
65 nm	65.30 nm
66 nm	66.30 nm
67 nm	67.30 nm
68 nm	68.31 nm
69 nm	69.30 nm
70 nm	70.30 nm
71 nm	71.30 nm
72 nm	72.30 nm
73 nm	73.31 nm
74 nm	74.30 nm
75 nm	75.30 nm
76 nm	76.30 nm
77 nm	77.30 nm
78 nm	78.30 nm
79 nm	79.30 nm
80 nm	80.31 nm

4.2.2 InAs layer thicknesses

Four different set of simulations have been made where the thicknesses of the InAs layers shown in figure 4.3 have been varied.

Bottom InAs layer

A set of simulations was made where the thickness of the bottom InAs layer was varied from 0 to 4 monolayers with a step size of 0.1 ML. The GaAs layer thickness was held constant at 70 nm and the top InAs layer was held constant at 2.0 ML.

Parts of the results can be seen in figure 4.9. In this figure it can be seen that the superlattice peaks from the InAs/GaAs peaks move towards lower angles as the bottom InAs thickness is increased. At 3.2 and 3.6 ML the diffraction peaks are weaker. This is due to a phase shift that occurs in the simulations between 2.4 and 4.0 ML. At 2.4 ML this phase shift appears at about 35°, and moves towards lower angles as the InAs bottom layer thickness increases. Figure 4.10 shows this phase shift more clearly. When the peak positions was calculated for simulations with a phase shift, the maximum points were used when the angle is lower than the position of the phase shift and the minimum points were used when the angle is higher than the position of the phase shift.

It can also be seen in figure 4.9 that the superlattice peaks disappear at 0.0 ML. They first appear at 0.1 ML, where they are very weak. The amplitude of the peaks then increases until 0.5 ML. This means the bottom InAs layer is needed for the superlattice peaks to occur.

The position of the zero-order peak has been estimated, and the results is presented in figure 4.11. There are two data sets shown in this figure, one where the position of the zero-order peak has been estimated by taking the average of the angular position of the -2 and +2 peaks in the simulations where both these peaks are visible, and one where where the actual position of the zero-order peak is shown in the simulations where it is visible. The zero-order peak seems to shift towards lower angles as the InAs layer thickness increases. There is one exception: The estimated zero-peak position seems to increase between 3.1 and 3.4 ML. This may be due to the zero-order peak being very weak in this area, making it harder to find the exact location of this peak and introducing an error source in the peak location estimate.

It can also be seen that the actual zero peak position is about 0.015–0.020° higher than the estimated peak position at 2.4–3.0 ML, but shifts much closer to the estimated zero-peak position at 3.7–4.0 ML. This might be due to what is sometimes called the *thin film effect*: When a thin epilayer that is strained is close to another, thicker epilayer, the interference between the reflected waves from the thin epilayer and the reflected waves from the thicker layer (e.g. the substrate) will lead to the XRD peak from the thin layer being shifted closer to the XRD peak of the thicker layer[18]. This effect is seen when the product $h \cdot e$ of the thickness h and the strain e of the thinnest layer is less than 0.5 nm, which is the case for the InAs layers. At 2.4–3.0 ML the zero-order peak is shifted towards the GaAs Bragg peak, but at 3.7–4.0 ML this effect disappears and the actual peak position is much closer to the estimated peak position.

The superlattice thickness was also estimated based on the diffraction peaks in the simulations. The results are shown in figure 4.12. As shown in this figure, the estimated superlattice thickness increases from 70.02 nm at 0.1 ML, via 70.30 nm at 2.0 ML to 70.60 nm at 4.0 ML.

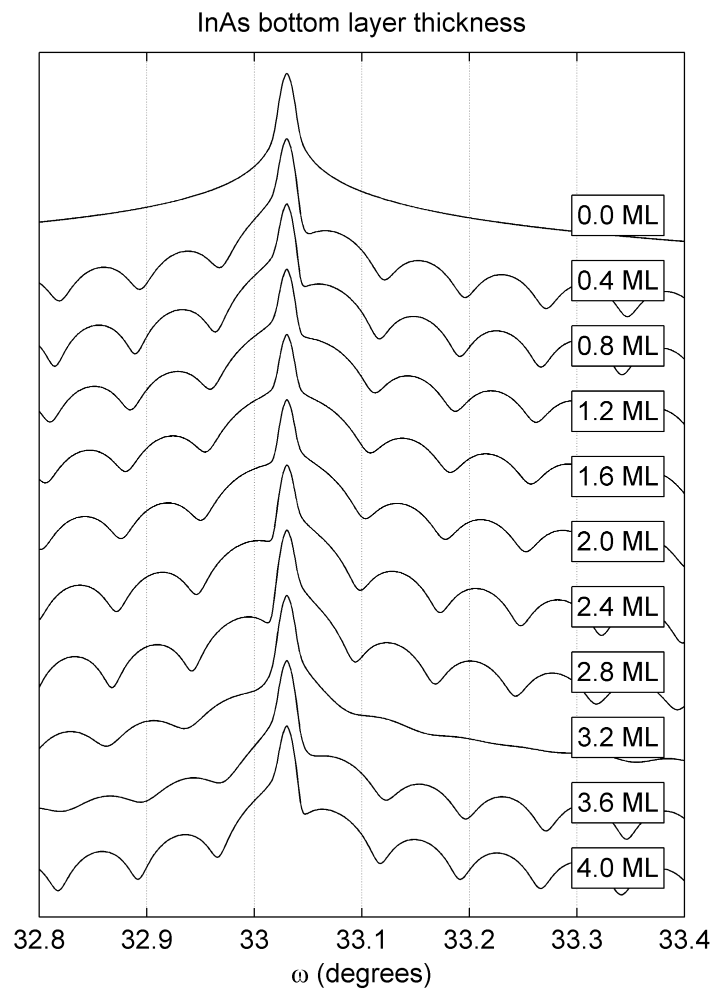

Figure 4.9: *Parts of the simulations with a varying InAs bottom layer thickness and the top layer held constant at 2.0 ML.*

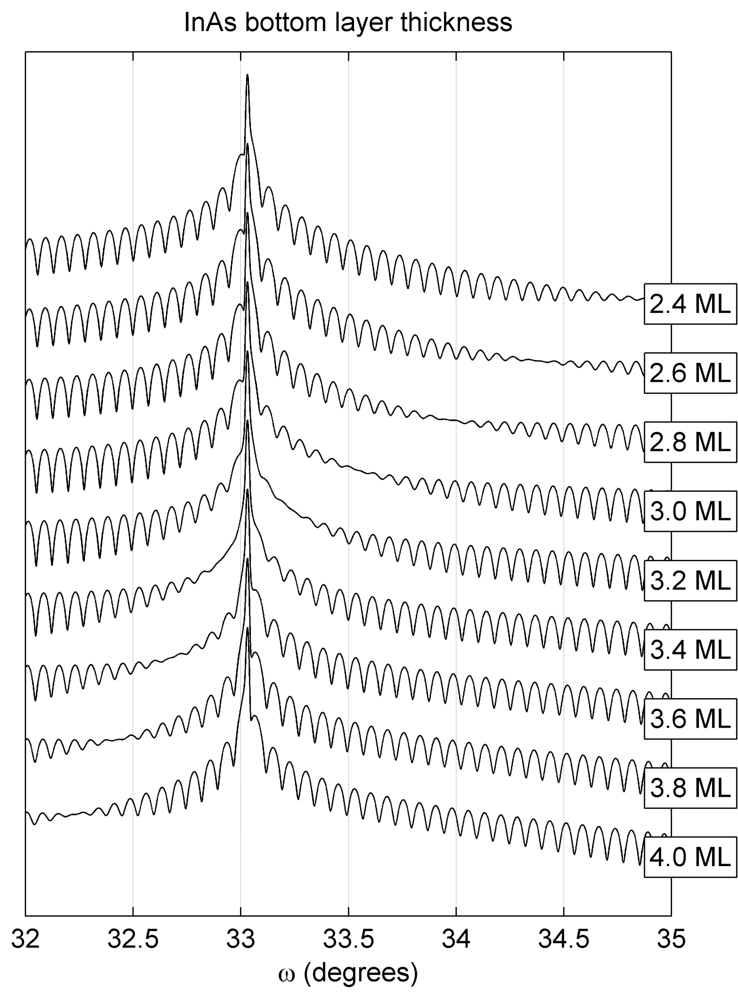

Figure 4.10: *A wider view on the simulations between 2.4 and 4.0 ML.*

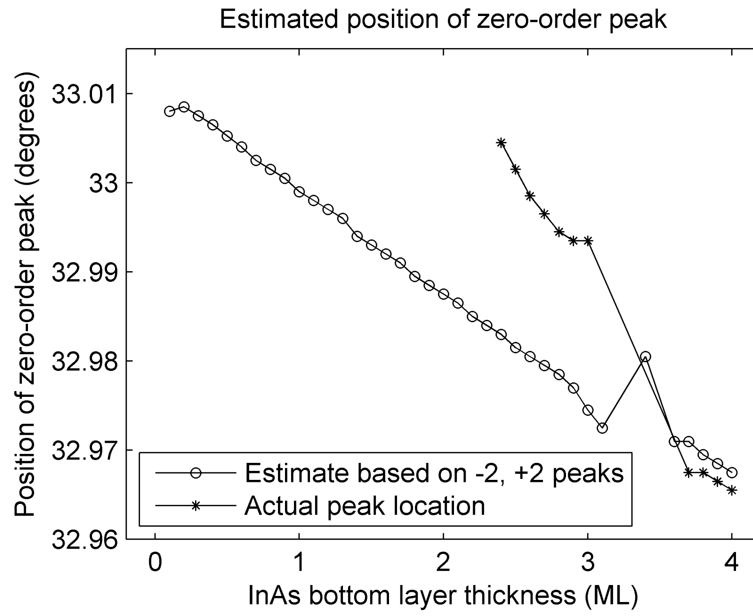

Figure 4.11: *Zero-order peak location as a function of InAs bottom layer thickness.*

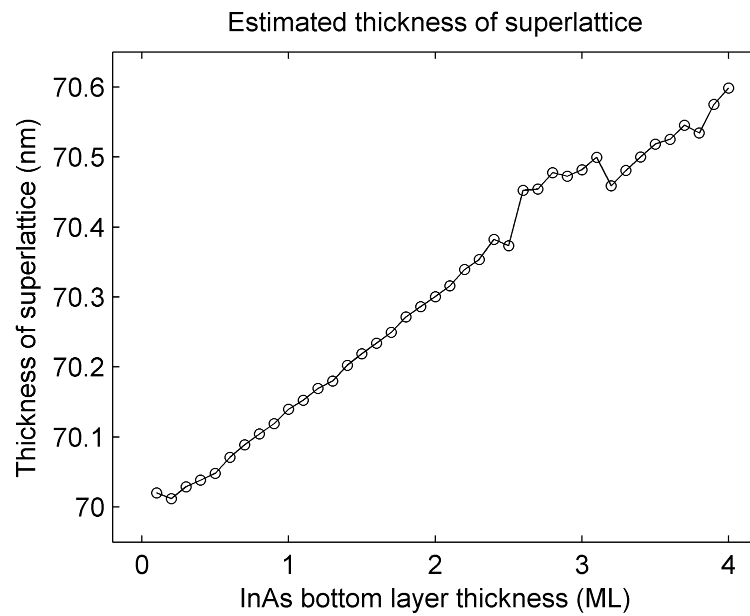

Figure 4.12: *Estimated superlattice thickness as a function of InAs bottom layer thickness.*

Top InAs layer

A set of simulations was made where the thickness of the top InAs layer was varied from 0 ML to 4 ML with 0.1 ML steps. The bottom InAs layer and the GaAs spacer were held constant at 2.0 ML and 70 nm, respectively.

Parts of the results can be seen in figure 4.13. From this figure it can be seen that the satellite peaks near the GaAs Bragg peak do not move significantly as the InAs top layer thickness increases.

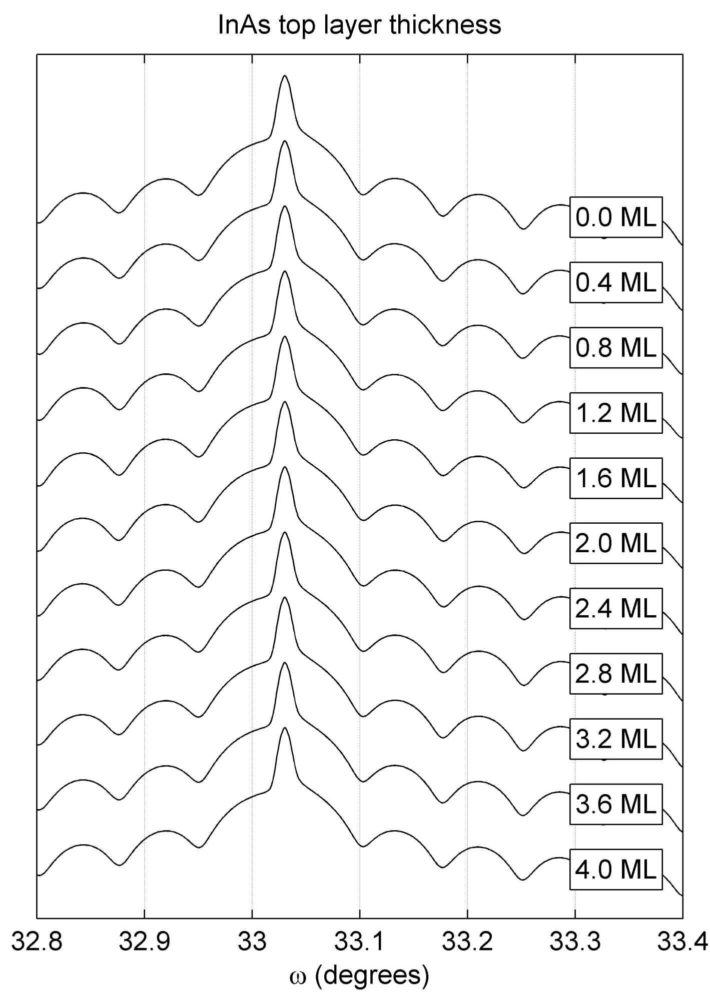

Figure 4.13: *Parts of the simulations with a varying InAs top layer thickness and the bottom layer held constant at 2.0 ML.*

The position of the zero-order peak was estimated by taking the average of the position of the -2 and +2 satellite peaks. The result can be seen in figure 4.14. From this figure it can be seen that the zero-order peak location does not change significantly. This suggests changes in the thickness of the top layer does not cause significant changes in the position of the satellite peaks.

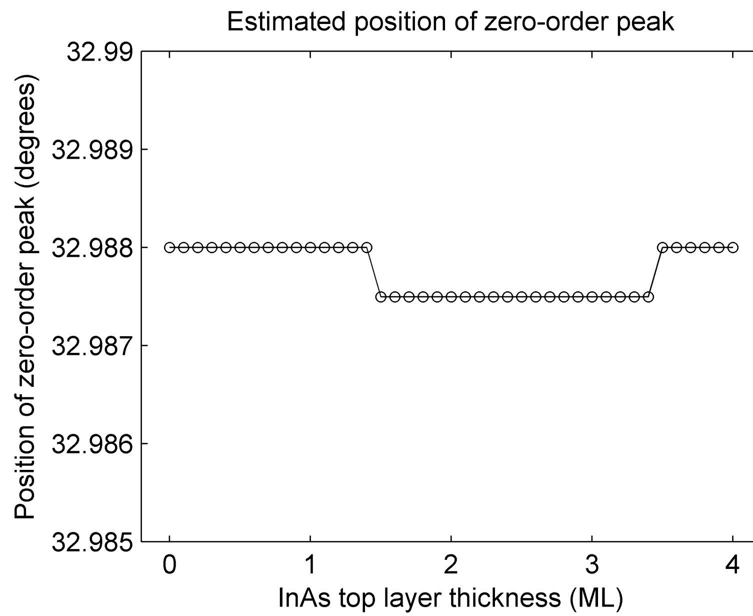

Figure 4.14: *Zero-order peak location as a function of InAs top layer thickness.*

The thickness of the superlattice has also been estimated based on the peak locations, and the results are shown in figure 4.15. From this figure it can be seen that the superlattice thickness does not increase linearly with the top InAs thickness as was expected, but has maximums at 0.8 ML (with a superlattice thickness of 70.60 nm) and 3.3 ML (with a superlattice thickness of 70.41 nm), and a minimum at 1.8 ML (with a superlattice thickness of 70.30 nm).

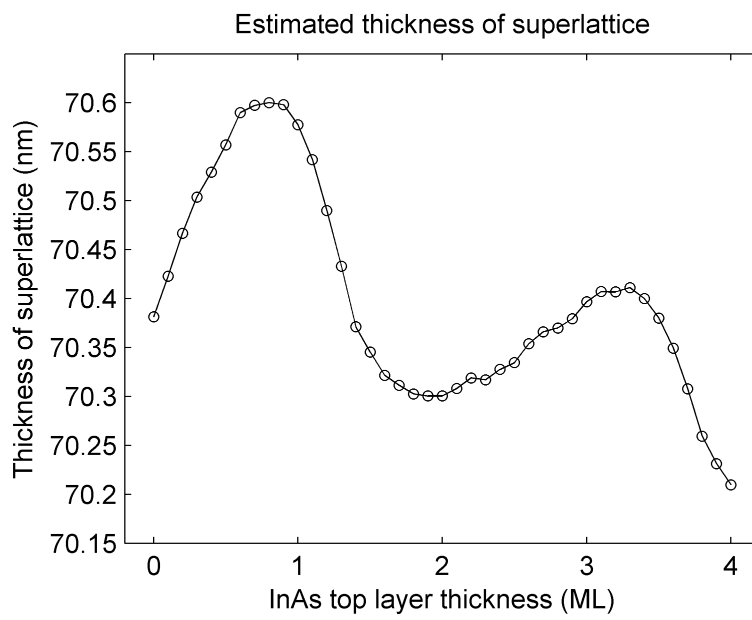

Figure 4.15: *Estimated superlattice thickness as a function of InAs top layer thickness.*

No top InAs layer

Another set of simulations was made with bottom InAs layer thickness varying from 0 to 4 ML. The simulations had a 70 nm GaAs spacer and no InAs top layer.

Parts of the results can be seen in figure 4.16. As can be seen from this figure, the peaks appear to shift toward lower angles as the thickness of the bottom InAs layer is increased. A phase shift appears at 3.2 and 3.6 ML. Also note how the superlattice peaks disappear when the bottom InAs layer is 0.0 ML thick.

The location of the zero-order peak has been estimated based on the location of the -2 and +2 peaks in the simulations where they are visible. The results are shown in figure 4.17. From this figure, it can be seen that the estimated zero-order peak position decreases linearly as the InAs layer thickness increases from 0.1 to 4.0 ML. There is one exception at 3.4–3.5 ML, which may be due to the -2 and +2 peaks being weak and harder to distinguish in this range, introducing an error source in the estimate of the peak location. It can also be seen that the actual zero peak position seems to be shifted towards the GaAs Bragg peak at 2.4–3.0 ML, possibly due to the thin film effect.

The thickness of the superlattice was also estimated based on the superlattice peak positions in the simulation. The results are shown in figure 4.18. As can be seen from this figure, the superlattice thickness increases from 70.10 nm at 0.1 ML, via 70.38 nm at 2.0 ML to 70.67 nm at 4.0 ML.

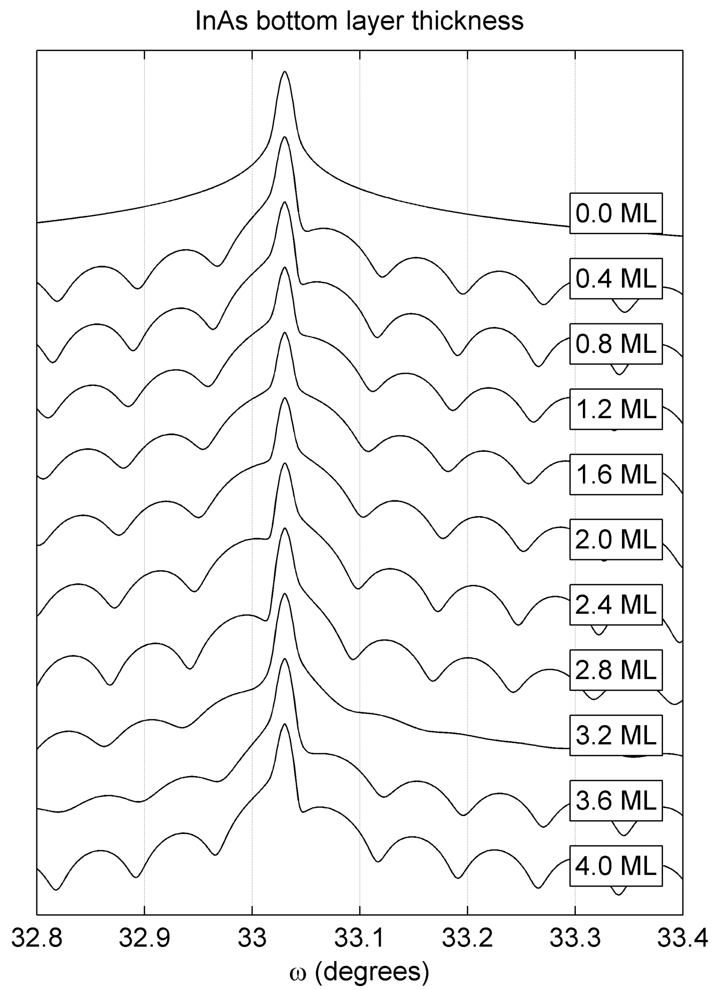

Figure 4.16: *Parts of the simulations with a varying InAs bottom layer thickness and no top layer.*

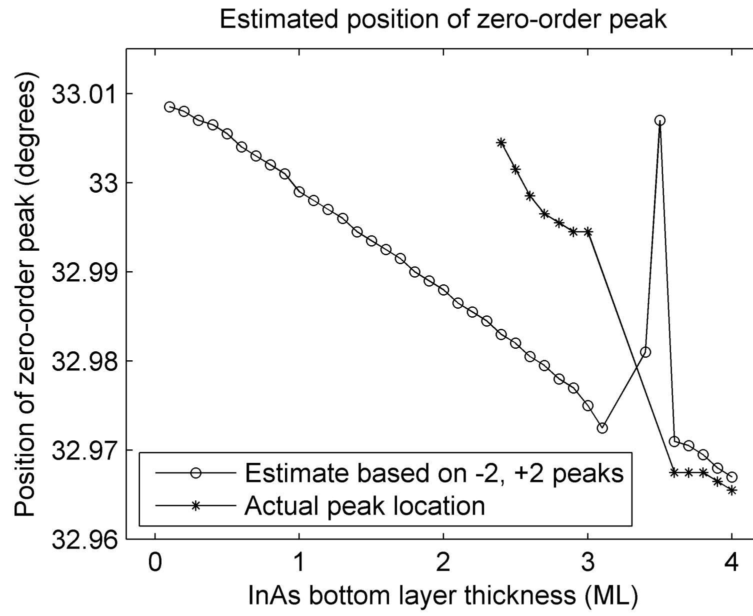

Figure 4.17: *Zero-order peak location as a function of InAs bottom layer thickness.*

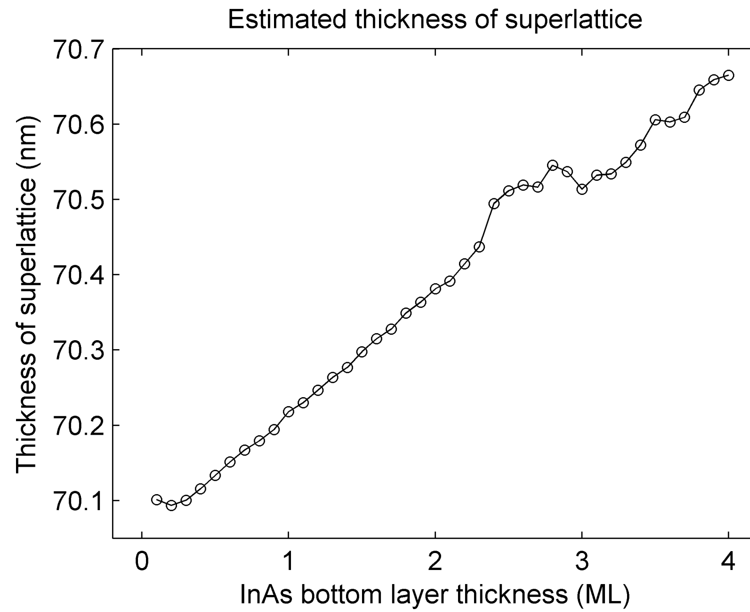

Figure 4.18: *Estimated superlattice thickness as a function of InAs bottom layer thickness.*

Both top and bottom InAs layer

A set of simulations was made where both the thicknesses of the top and the bottom InAs layers were varied from 0.0 to 4.0 ML. The thicknesses of these two layers were equal at all times, while the GaAs spacer layer was held constant at 70 nm.

Parts of the result can be seen in figure 4.19. The superlattice peaks seem to shift towards lower angles with increasing InAs layer thickness. The same kind of phase shift that was observed for the other simulations with varying bottom layer thickness, can also be seen here at 3.2 and 3.6 ML. The superlattice peaks also seem to disappear when the InAs layer thicknesses are 0.0 ML.

An estimate of the zero-order peak location can be seen in figure 4.20. In this figure the general trend is that the zero-order peak shifts towards lower angles as the InAs layer thickness increases. It can be seen that the zero-order peak is shifted towards the GaAs Bragg peak at 2.4–3.0 ML, possibly due to the thin film effect.

Estimates was also made of the superlattice thicknesses as shown in figure 4.21. The results show that the estimated superlattice thickness does not increase linearly with the InA layer thicknesses as was expected, but has maximums at 1.0 ML (with a superlattice thickness of 70.41 nm) and 3.4 ML (with a superlattice thickness of 70.61 nm) and a minimum at 1.5 ML (with a superlattice thickness of 70.26 nm).

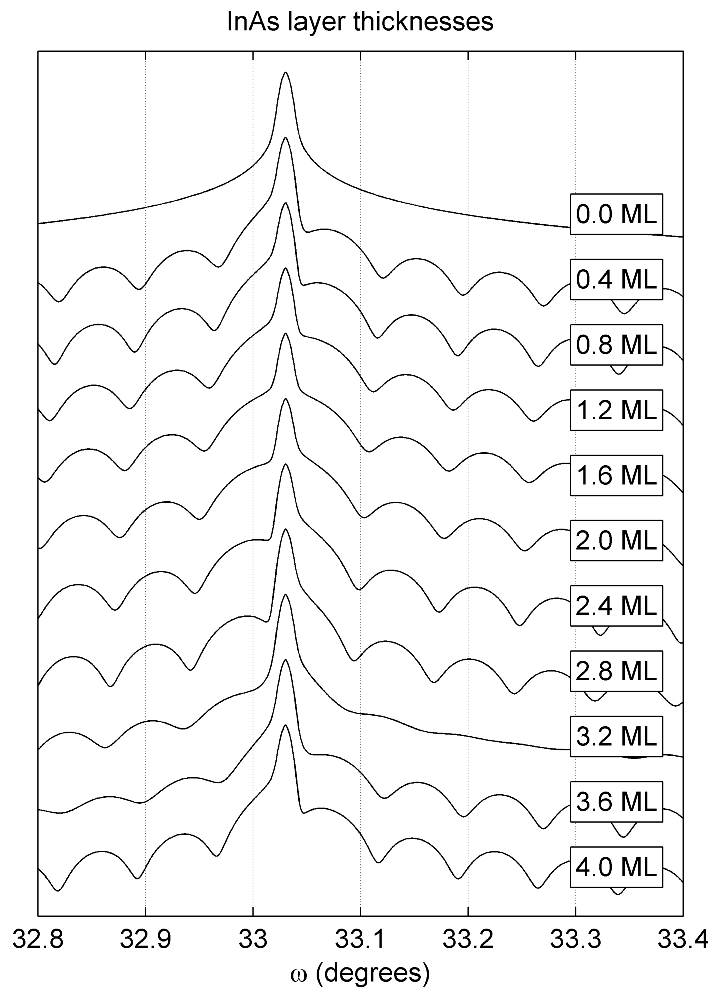

Figure 4.19: *Parts of the simulations with varying InAs top and bottom layer thicknesses.*

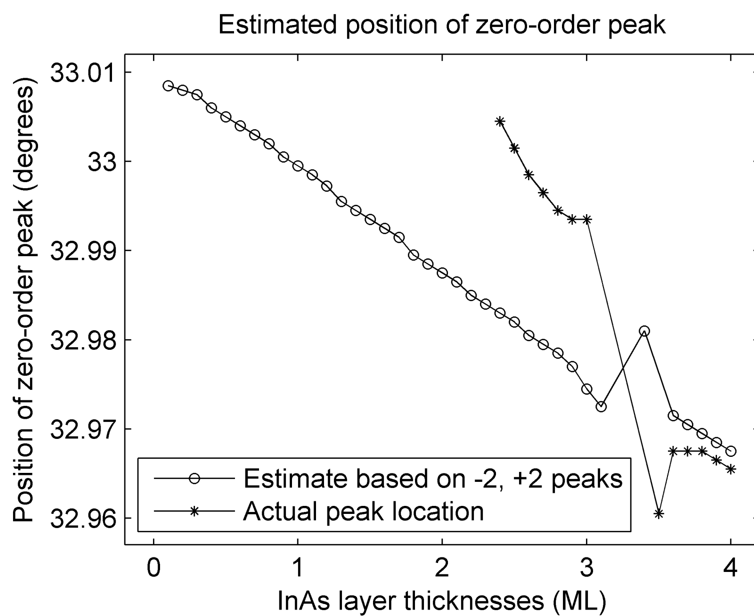

Figure 4.20: *Zero-order peak location as a function of InAs layer thicknesses.*

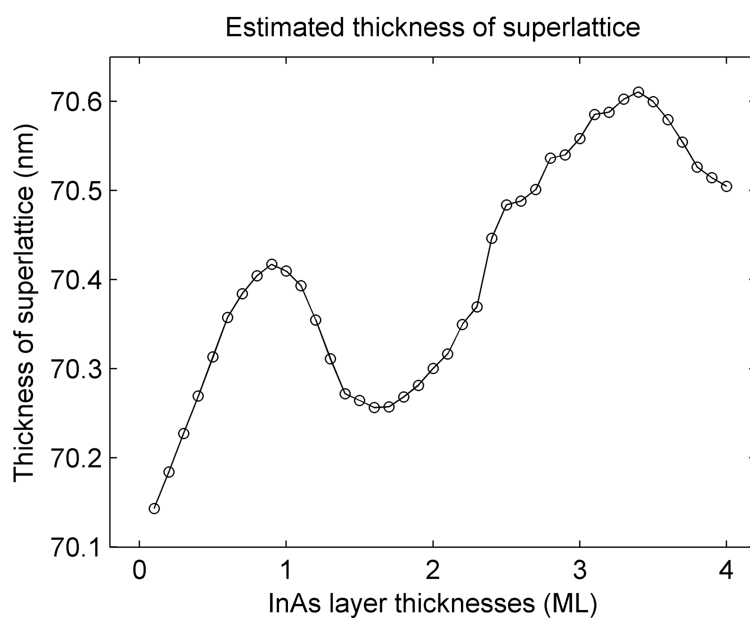

Figure 4.21: *Estimated superlattice thickness as a function of InAs bottom layer thicknesses.*

4.2.3 Segregation

When a layer of InAs is overgrown (capped) with a GaAs layer, some of the In atoms will be exchanged with the incoming Ga atoms. The In thus segregates to the top-most layer when the growth takes place. Three different cases of segregation have been simulated.

Case 1

Segregation has been modelled using a constant segregation rate r, which determines how many In atoms are exchanged with Ga in the monlayer above. An amount r of In from the upper monolayer of the InAs layer moves into the Ga layer above and is replaced by Ga, while $1-r$ remain in the original InAs monolayer. In the following monolayer above the amount of In is then $r(1-r)$, as r is taken from the layer below and a $1-r$ remainder of it is left in this layer as the rest segregates into the next layer above. The amount of InAs in the following monolayer above that is $r^2(1-r)$, etc. as shown in figure 4.22.

This has been simulated in LEPTOS by using a finite number of $Ga_{1-x}In_xAs$ layers with x being the amount of InAs in each monolayer. The amount of InAs in any given layer k is $r^k(1-r)$ except for the last layer n with segregation where the amount of InAs is r^n.

Then, by using the geometric sum formula:

$$\sum_{k=1}^{n} q^{k-1} = \frac{1-q^n}{1-q}$$

the total amount of InAs in all monolayers can be shown to be:

$$(1-r)\sum_{k=1}^{n} r^{k-1} + r^n = (1-r)\frac{1-r^n}{1-r} + r^n = 1$$

In other words, the total amount of InAs is preserved even though it is distributed across several monolayers.

Segregation with a segregation rate of 30% was simulated for the bottom InAs layer in Leptops. Up to 9 layers of segregation was simulated, because for ten layers and above the amount of InAs segregated becomes too small to enter in LEPTOS. The thickness of the monolayers that InAs segregates into was calculated by finding the average lattice constant weighted on the amounts of InAs and GaAs in the monolayer. The total amount of GaAs in the spacer and the segregated layers was kept constant at 70 nm.

Parts of the results can be seen in figure 4.23. As shown in this figure, there are no significant changes in the position of the peaks near the Bragg peak as segregation is introduced.

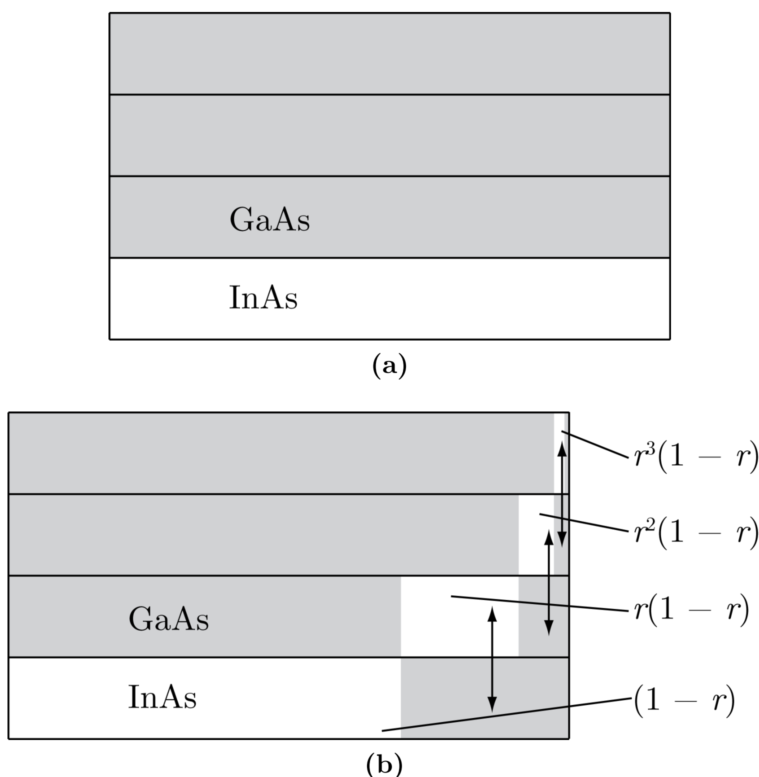

Figure 4.22: *(a) InAs/GaAs structure with one monolayer of InAs and three monolayers of GaAs. (b) The same structure with segregation of In during growth (r = 0.3%). The bottom layer has 70% InAs, where the rest has segregated into the layers above. The next layers have 21%, 6.3% and 1.89% InAs, respectively. Then there is a remainder of 0.81%, which segregates into additional layers above.*

A set of simulations was also made similar to the segregation simulation described above, but where the number of layers is constant at 5 and the segregation rate varies from 0% (no segregation) in steps of 5% to 50%. Parts of the results can be seen in figure 4.24. As shown in this figure, no significant changes occur in the position of the satellite peaks near the GaAs Bragg peak as the segregation rate increases.

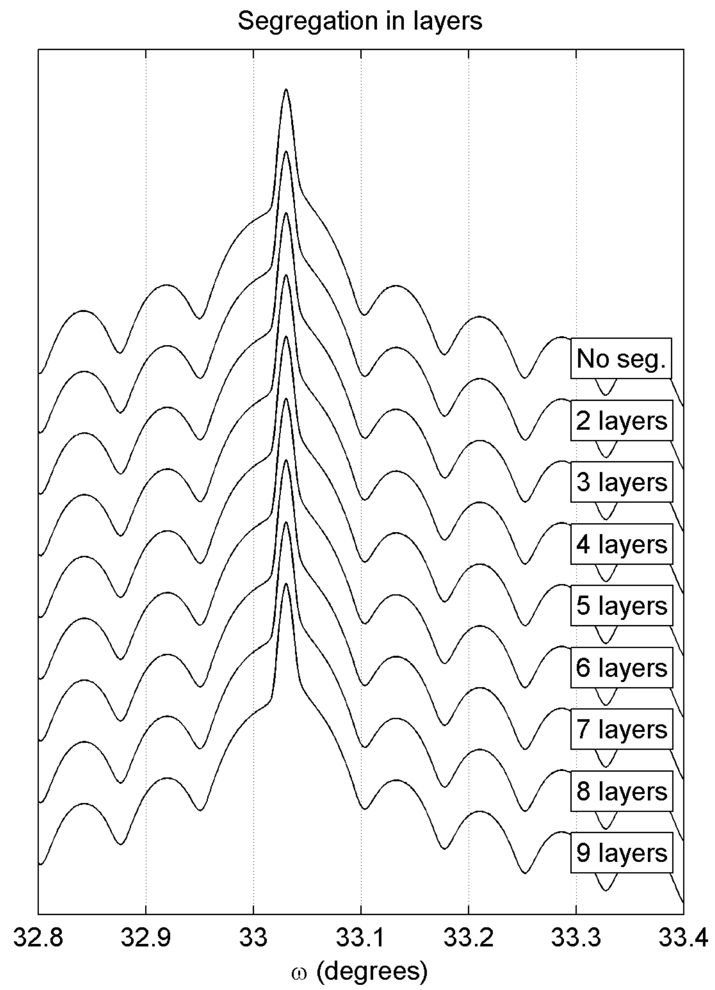

Figure 4.23: *Simulated for segregation with a segregation rate of 30%.*

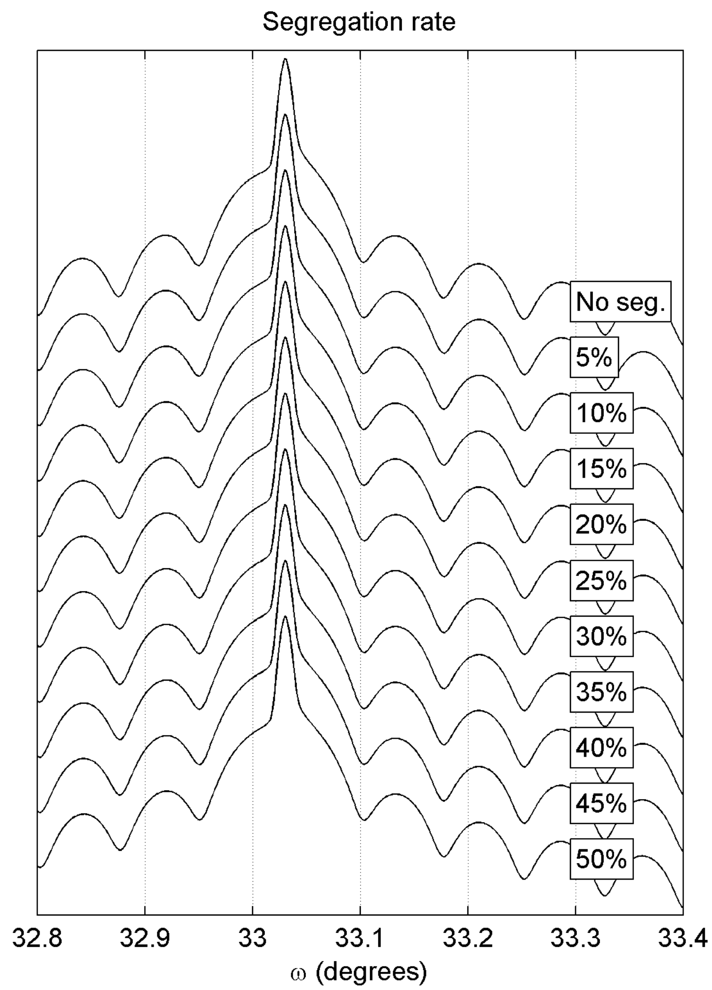

Figure 4.24: *Simulations with segregeation in 5 layers, for increasing segregation rate from* $r = 0\%$ *to* $r = 50\%$.

Case 2

A set of simulations were made with a rougher model of segregation. In these simulations, the top monolayer of the bottom InAs layer is mixed with the above GaAs layer, creating a $Ga_{(1-x)}In_xAs$ alloy. The total amount of InAs in the bottom layer and the alloy was kept constant at 2.0 ML, and the total amount of GaAs in the alloy and the spacer was kept constant at 70 nm. The thickness of the top InAs layer was kept constant at 2.0 ML. The amount of InAs in the alloy varied from 100% to 50%, and the thickness of the GaAs spacer was reduced as the amount of GaAs in the alloy increased to keep the total amount of GaAs constant, as shown in table 4.2 and illustrated in figure 4.25. The results can be seen in figure 4.26. As shown in this figure, no significant changes occurs in the position or separation of the peaks near the GaAs Bragg peak as the thickness of the alloy increases.

Table 4.2: *Alloy and GaAs spacer thicknesses for varying amount of InAs.*

InAs percentage	**Alloy thickness**	**GaAs spacer thickness**
100%	0.33 nm	70.00 nm
95%	0.34 nm	70.00 nm
90%	0.35 nm	69.99 nm
85%	0.37 nm	69.97 nm
80%	0.38 nm	69.96 nm
75%	0.40 nm	69.94 nm
70%	0.41 nm	69.93 nm
65%	0.42 nm	69.92 nm
60%	0.44 nm	69.90 nm
55%	0.45 nm	69.89 nm
50%	0.47 nm	69.87 nm

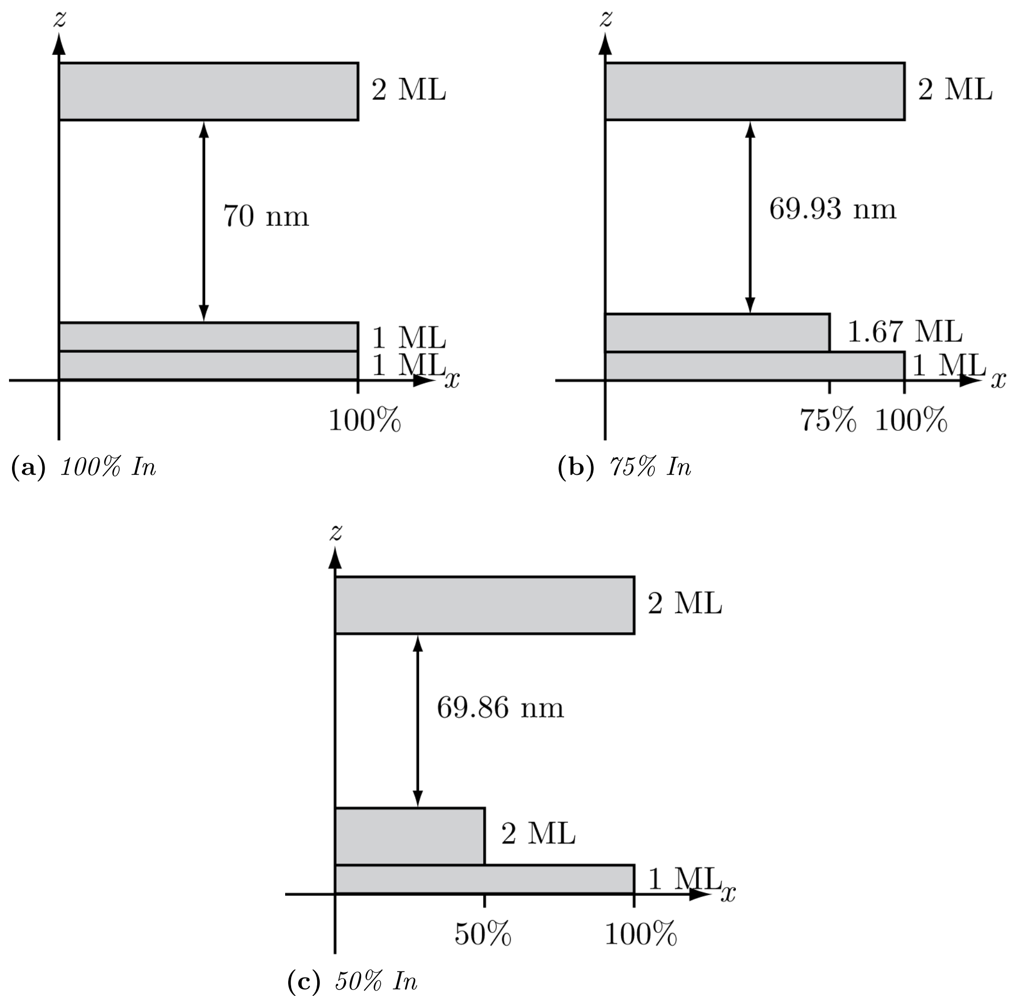

Figure 4.25: *Schematic drawings of the InAs content along the growth direction z. x is the InAs content and $1-x$ is the GaAs content.*

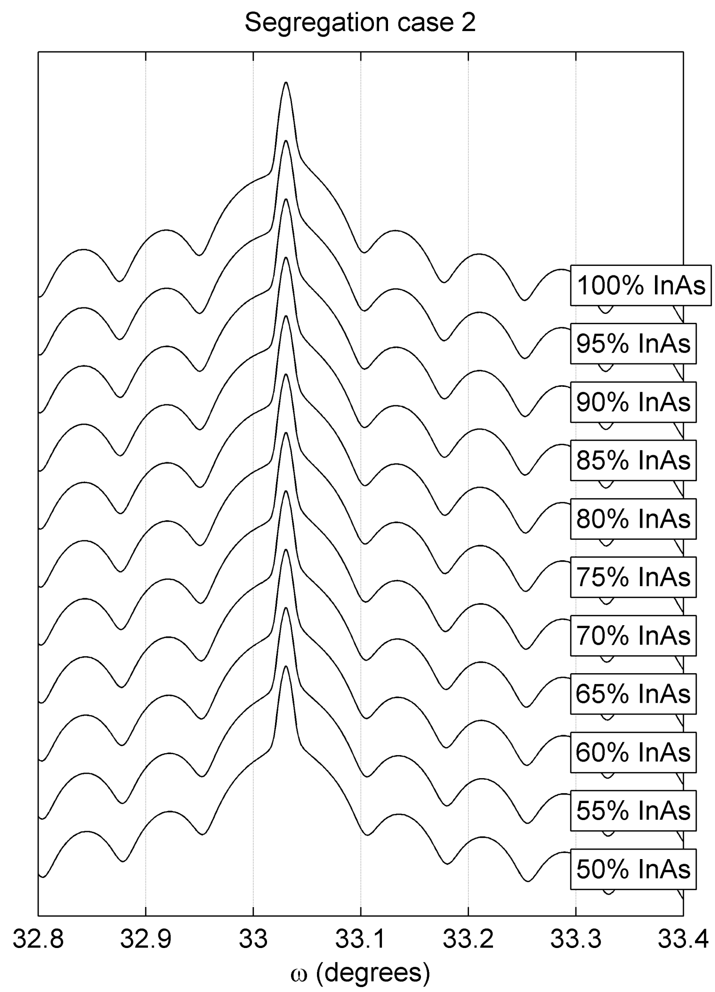

Figure 4.26: *Simulations of segregation with varying amount of InAs in alloy.*

Case 3

Four simulations were made to investigate extreme cases of segregation, as illustrated in figure 4.27:

- *Reference*: A simulation with 2 ML InAs bottom layer, 70 nm GaAs spacer and 2 ML InAs top layer.
- *Averaged*: The InAs bottom layer and GaAs spacer layer in the reference simulation were replaced with one layer where the InAs content was evened out across the entire layer (so that the layer was 0.92% InAs). This layer had the exact same amount of InAs and GaAs as the InAs and GaAs layers it replaced. The 2 ML InAs layer on top was unchanged.
- *Narrow triangular*: The bottom InAs layer in the reference simulation was replaced with a layer with a triangular distribution of GaAs and InAs. At the bottom of this layer there was 100% InAs, and at the top there was 0% InAs. This layer had a thickness equivalent to two monolayers of InAs plus two monolayers of GaAs. The GaAs spacer layer thickness was reduced by two monolayers to compensate for the GaAs in the layer below. The 2 ML InAs layer on top was unchanged.
- *Broad triangular*: The bottom InAs layer and the GaAs spacer in the reference simulation were replaced by a layer with a triangular GaAs-InAs distribution, where there was 1.84% InAs on the bottom and 0% InAs on the top. The 2 ML InAs layer on top was unchanged.

Part of the results can be seen in figure 4.28. Here it can be seen that the "narrow triangular" simulation is very similar to the reference simulation. The "averaged" simulation and the "broad triangular" simulation are different from the reference simulation, but these two simulations are similar to each order. The zero-order peak in these two simulations seems to have shifted towards a lower angle compared to the reference simulation. The "averaged" simulation seems to have a very weak peak amplitude for the superlattice peaks, which is possibly due to the low InAs content in the InAs/GaAs layer making the interface to the GaAs substrate less abrupt. In the "broad triangular" simulation the peaks seem to have a larger amplitude, but they are still weaker than in the reference simulation. This is possibly because the InAs content in this simulation has been increased compared with the "averaged" simulation, making the interface to the GaAs substrate more abrupt and providing a stronger reflection from the interface between the InAs/GaAs layer and the substrate.

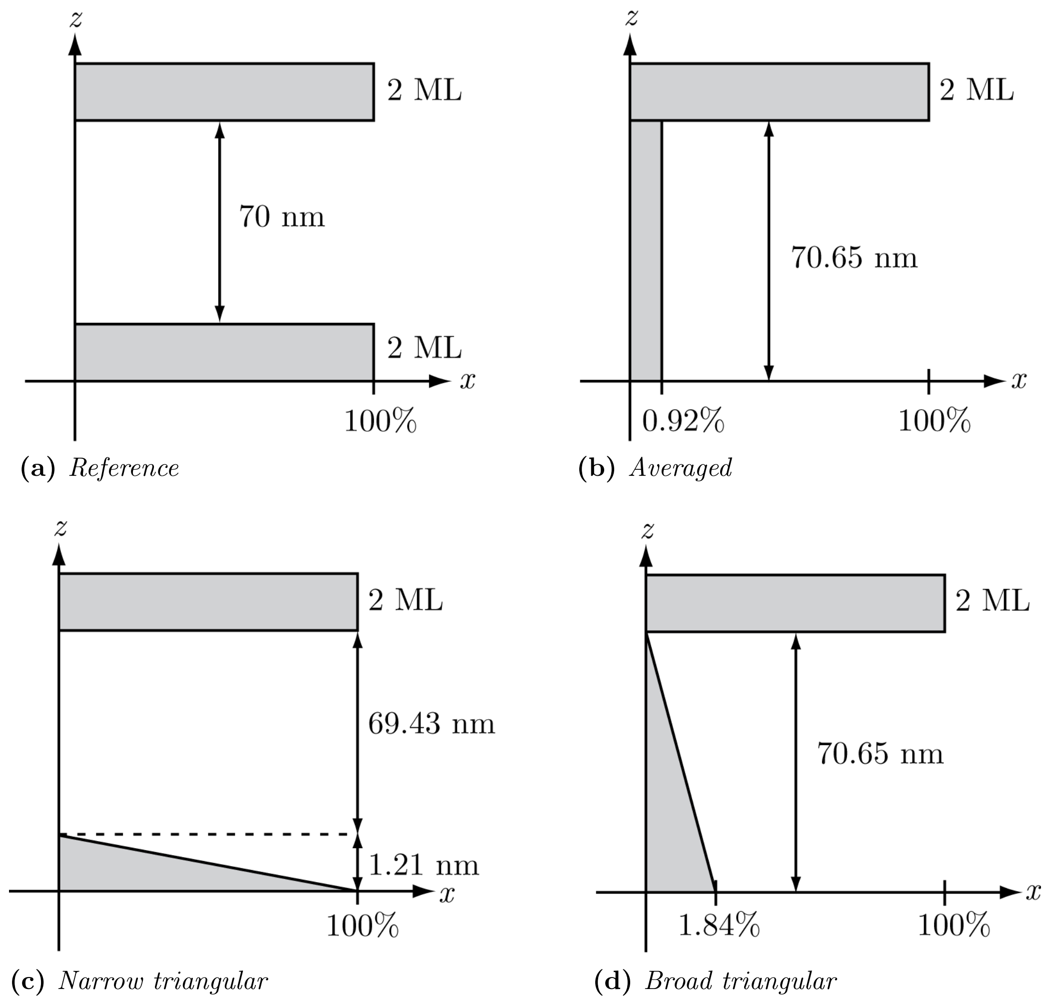

Figure 4.27: *Schematic drawings of the InAs content along the growth direction z. x is the InAs content and $1 - x$ is the GaAs content.*

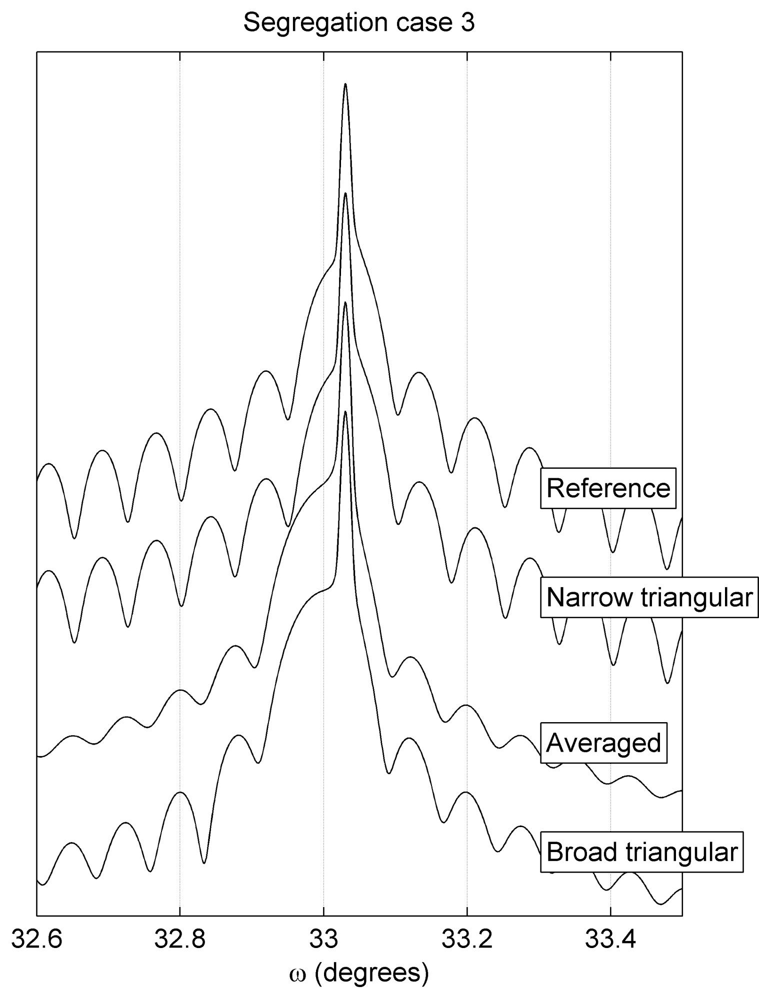

Figure 4.28: *Simulations with different InAs distributions.*

4.2.4 Intermixing and segregation

Eleven simulations were made, based on a structure with a GaAs substrate, 1 ML of InAs, 70 nm of GaAs and 2 ML of InAs. The lower monolayer of InAs is then mixed with GaAs from the substrate and/or from the GaAs layer above to simulate layer intermixing and segregation effects. This was modelled by creating three mixed InAs/GaAs monolayers in the bottom, and varying the InAs/GaAs content in these layers as shown in figure 4.29. In some simulations the GaAs in the alloy is taken from the substrate (intermixing) and in some simulation the GaAs in the alloy is taken from the spacer layer (segregation). The thicknesses of these layers are calculated from the average lattice constant of InAs and GaAs weighted on the amounts of these materials. The total amount of InAs in the alloys always equals 1 ML, and the total amount of GaAs in the spacer and the alloys always equals 70 nm. Simulations have been made as shown in table 4.3.

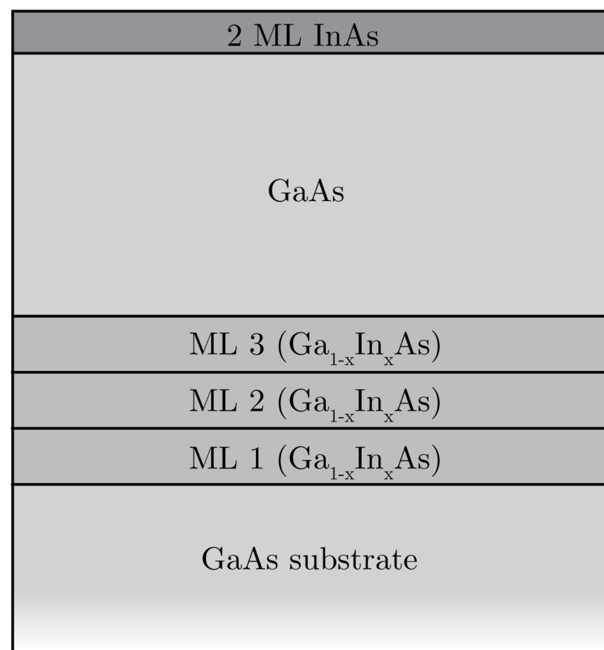

Figure 4.29: *A schematic drawing of the structure used in InAs/GaAs intermixing simulations.*

Parts of results can be seen in figure 4.30. It can be seen that the results for various simulations are very similar.

For all simulations the location of the zero-order peak and the superlattice thickness was estimated. The zero-order peak location was estimated based

Table 4.3: *Simulations of InAs/GaAs intermixing.*

		ML 1	ML 2	ML 3
	InAs content	100%	0%	0%
Simulation 1	**GaAs comes from**	-	Spacer	Spacer

		ML 1	ML 2	ML 3
	InAs content	50%	50%	0%
Simulation 2a	**GaAs comes from**	Substrate	Substrate	Spacer
Simulation 2b	**GaAs comes from**	Spacer	Spacer	Spacer

		ML 1	ML 2	ML 3
	InAs content	90%	10%	0%
Simulation 3a	**GaAs comes from**	Substrate	Substrate	Spacer
Simulation 3b	**GaAs comes from**	Substrate	Spacer	Spacer
Simulation 3c	**GaAs comes from**	Spacer	Spacer	Spacer

		ML 1	ML 2	ML 3
	InAs content	10%	90%	0%
Simulation 4a	**GaAs comes from**	Substrate	Substrate	Spacer
Simulation 4b	**GaAs comes from**	Substrate	Spacer	Spacer

		ML 1	ML 2	ML 3
	InAs content	10%	80%	10%
Simulation 5a	**GaAs comes from**	Substrate	Substrate	Substrate
Simulation 5b	**GaAs comes from**	Substrate	Substrate	Spacer
Simulation 5c	**GaAs comes from**	Substrate	Spacer	Spacer

on the location of the -2 and +2 peaks. The results are shown in table 4.4. As can be seen from this table, the zero-order peak location seems to be constant. This is because any changes in the InAs/GaAs composition are too small to cause a noticeable change of the peak location. Also the estimated superlattice thickness seem to be higher in the simulations where GaAs is taken from the substrate, compared to the simulations where GaAs is taken from the spacer only. This can be explained as the total amount of GaAs in the superlattice is increased in the simulations where GaAs is taken from the substrate simulations, leading to an increase in the separation of the satellite peaks.

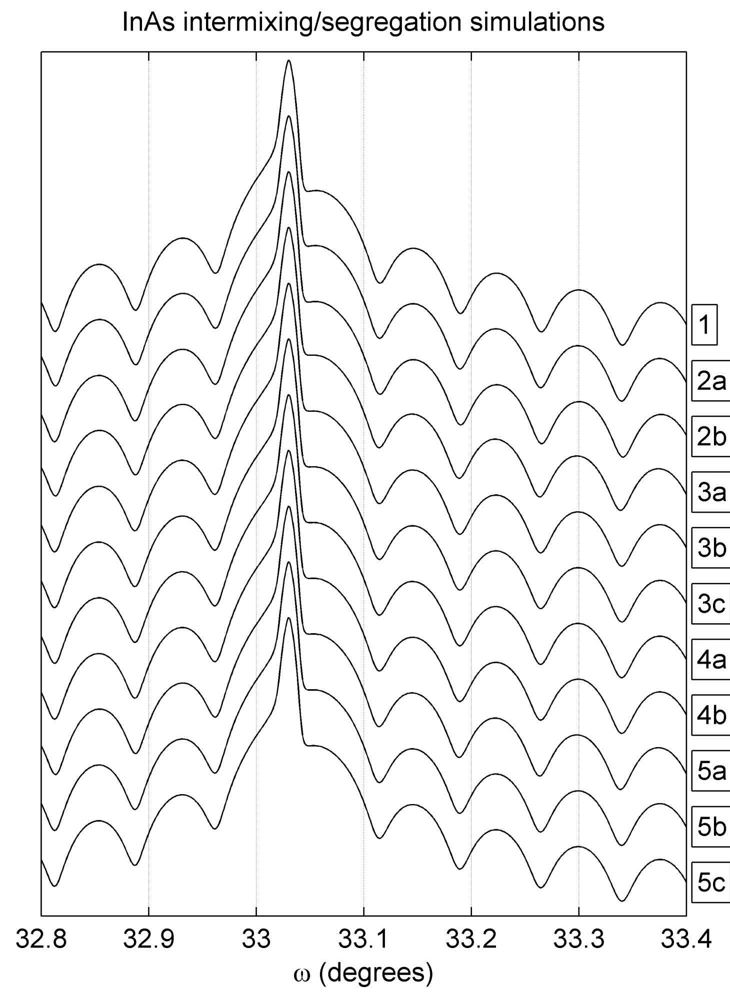

Figure 4.30: *Parts of of InAs/GaAs intermixing simulations.*

Table 4.4: *Estimated zero-order peak location and superlattice thickness.*

Simulation	Estimated zero-order peak location	Estimated superlattice thickness
1	33.000	70.12
2a	33.000	70.27
2b	33.000	69.99
3a	33.000	70.40
3b	33.000	70.14
3c	33.000	70.12
4a	33.000	70.15
4b	33.000	70.13
5a	33.000	70.43
5b	33.000	70.17
5c	33.000	70.11

4.2.5 Summary

In the simulations periodic satellite peaks were observed in addition to the GaAs Bragg peak. The InAs/GaAs structure is not a superlattice, as it is not a repeated structure. Still the superlattice theory can be used as an approximation to what is actually seen in the simulation. What has been interpreted as superlattice peaks in the simulations is most likely diffraction fringes from the epilayers. When the superlattice thickness as a function of the top layer thickness was calculated, a complex, periodic interaction was seen between the top layer thickness and the superlattice thickness. Also in some of the simulations a phase shift was seen, which suggests the diffraction peaks observed in the simulations is actually a sum of several different sets of diffraction peaks with slightly different period.

These results suggest there are interactions between x-rays scattered from the different layers that can only be explained using *dynamical diffraction theory* where interference effects between reflections from different layers are taken into consideration. Explaining the dynamical diffraction theory is beyond the scope of this thesis.

The most important conclusions that can be drawn from the simulations are:

- The angular separation of the XRD satellite peaks depends mainly on the GaAs layer thickness.
- The position of the zero-order satellite peak depends mainly on the thickness of the bottom InAs layer.
- Segregation does not seem to affect the XRD curve significantly, as long as a pure InAs layer is still present.
- Intermixing does seem to cause a change in the angular separation of the satellite peaks.
- An abrupt InAs/GaAs interface at the bottom of the InAs/GaAs bilayer structure is needed for the satellite peaks to show.

Chapter 5

X-ray diffraction measurements

In this chapter the results from the x-ray diffraction measurements are presented, analysed and discussed. In section 5.1 the measurements are presented, in section 5.2 curve fits are presented, in section 5.3 the superlattice thickness is calculated on basis of the results and finally in section 5.4 the results are discussed.

5.1 Measurement results

Sample *586-3* was grown using MBE, and has nominally the structure presented in figure 5.1. This sample was grown without rotation, which means the thickness of the thin film layers is expected to vary across the wafer depending on the distance from source, as described in section 4.1.

XRD measurements were done on this sample. A total of 13 measurements were made on the sample, as shown in figure 5.2. These measurements are spaced by 0.5 cm. The temperature varied between 29° and 30° Celsius during the measurements. EVA software from Bruker-AXS was used to search for peaks in the measurement results with the following settings: width = 0.02, threshold = 1. The results are shown in table 5.1. All the measurement results were offset so that the GaAs Bragg peak appear in the same location as in the simulations, to make comparisons between the individual results and between the results and simulations easier. The measurement results are shown in figure 5.3.

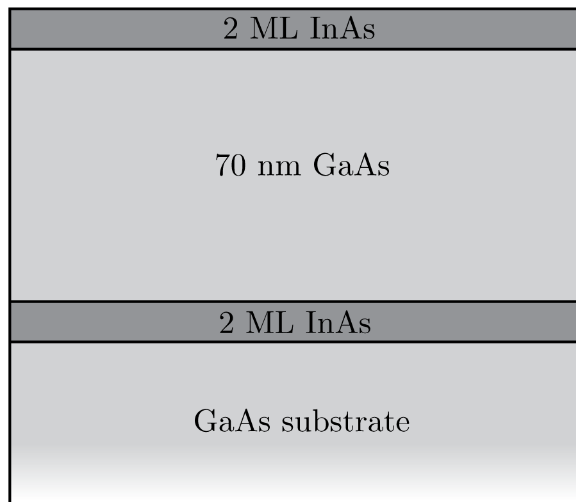

Figure 5.1: *Schematic drawing of the structure grown in MBE.*

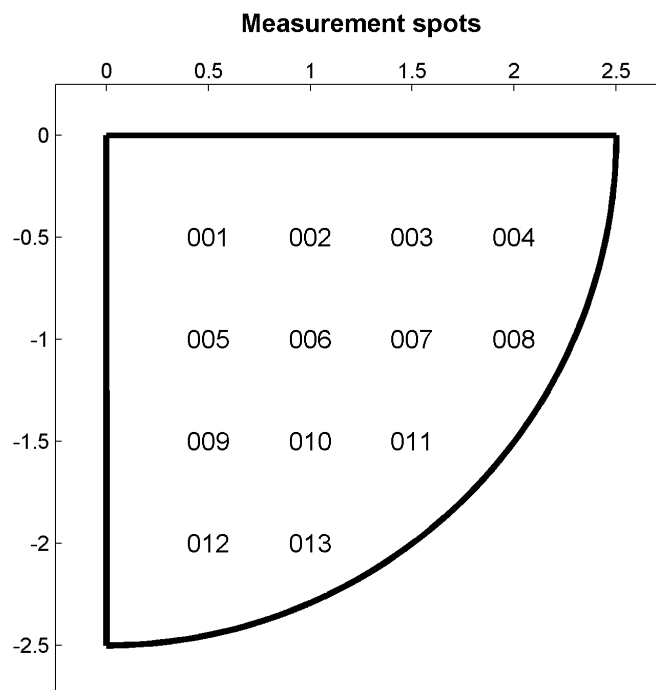

Figure 5.2: *Measurement spots for sample 586-3. Spot 001 is 5 mm from the edge in both directions, and all spots are spaced by 5 mm.*

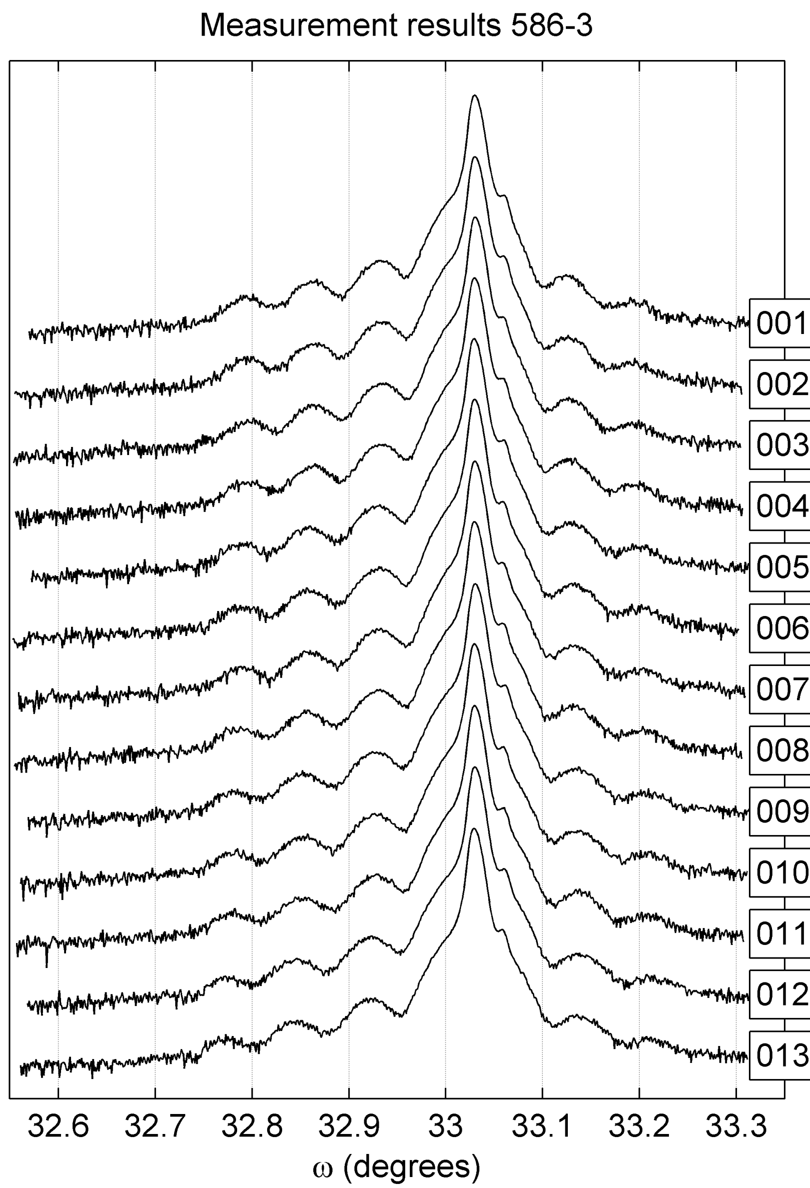

Figure 5.3: *Measurement results for sample 586-30.*

Table 5.1: *Peak search results.*

Peak order	-2	-1	1	2
001	32.8645	32.9330	33.0601	33.1211
002	32.8646	32.9347	33.0597	33.1242
003	32.8633	32.9351	33.0597	33.1246
004	32.8650	32.9346	33.0593	33.1274
005	32.8589	32.9301	33.0593	33.1281
006	32.8563	32.9329	33.0590	33.1309
007	32.8564	32.9315	33.0597	33.1321
008	32.8568	32.9326	33.0593	33.1314
009	32.8511	32.9257	33.0606	33.1343
010	32.8575	32.9294	33.0594	33.1306
011	32.8477	32.9270	33.0601	33.1371
012	32.8461	32.9233	33.0596	33.1357
013	32.8415	32.9236	33.0594	33.1325

5.2 Curve fitting

Manual curve fittings were made for all simulations. The curve fittings were made by simulating a structure based on the one seen in figure 5.1 using LEPTOS software, and varying the thicknesses of the bottom InAs layer and the GaAs spacer until the peaks in the simulation coincided with the visible peaks in the measurement results. The top InAs layer was kept constant at 2.0 ML. First the thickness of the GaAs layer was held constant while the thicknesses of the InAs layers were varied with 0.1 ML steps until the best possible fit was found, then the thicknesses of the InAs layers were held constant while the thickness of the GaAs layer was varied with 1 nm steps until the best possible fit was found, then the GaAs layer was kept constant again while the InAs layers were varied etc. until stable values were found for the thicknesses of the GaAs and InAs layers. Maximum and minimum thickness values were found for all curve fittings. An example is shown from the measurement in the 001 position in figure 5.4.

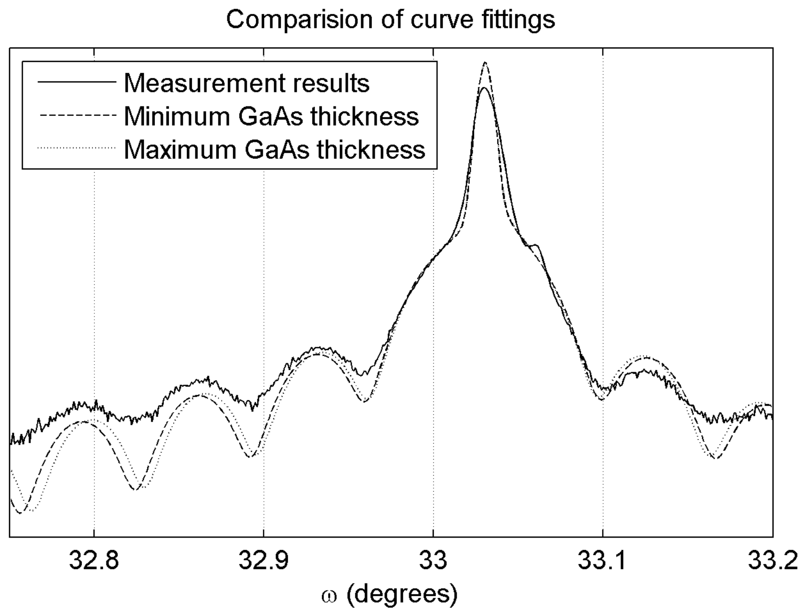

Figure 5.4: *Comparision of curve fittings for measurement in position 001.*

The results from the curve fittings are shown in tables 5.2 and 5.3 and illustrated in figures 5.5 and 5.6 for GaAs and in figures 5.7 and 5.6 for InAs.

Table 5.2: *Results from curve fitting for GaAs.*

Measurement	GaAs minimum	GaAs average	GaAs maximum
001	77.0 nm	78.0 nm	79.0 nm
002	78.0 nm	78.5 nm	79.0 nm
003	77.0 nm	78.0 nm	79.0 nm
004	76.0 nm	77.0 nm	78.0 nm
005	74.0 nm	75.5 nm	77.0 nm
006	73.0 nm	74.0 nm	75.0 nm
007	73.0 nm	74.5 nm	76.0 nm
008	73.0 nm	74.5 nm	76.0 nm
009	71.0 nm	72.0 nm	73.0 nm
010	72.0 nm	72.5 nm	73.0 nm
011	70.0 nm	71.0 nm	72.0 nm
012	69.0 nm	70.0 nm	71.0 nm
013	69.0 nm	70.0 nm	71.0 nm

Table 5.3: *Results from curve fitting for InAs.*

Measurement	InAs minimum	InAs average	InAs maximum
001	1.70 ML	1.80 ML	1.90 ML
002	1.70 ML	1.80 ML	1.90 ML
003	1.60 ML	1.70 ML	1.80 ML
004	1.50 ML	1.60 ML	1.70 ML
005	1.50 ML	1.70 ML	1.90 ML
006	1.30 ML	1.50 ML	1.70 ML
007	1.40 ML	1.55 ML	1.70 ML
008	1.20 ML	1.40 ML	1.60 ML
009	1.10 ML	1.30 ML	1.50 ML
010	1.10 ML	1.30 ML	1.50 ML
011	1.00 ML	1.15 ML	1.30 ML
012	1.30 ML	1.45 ML	1.60 ML
013	1.50 ML	1.70 ML	1.90 ML

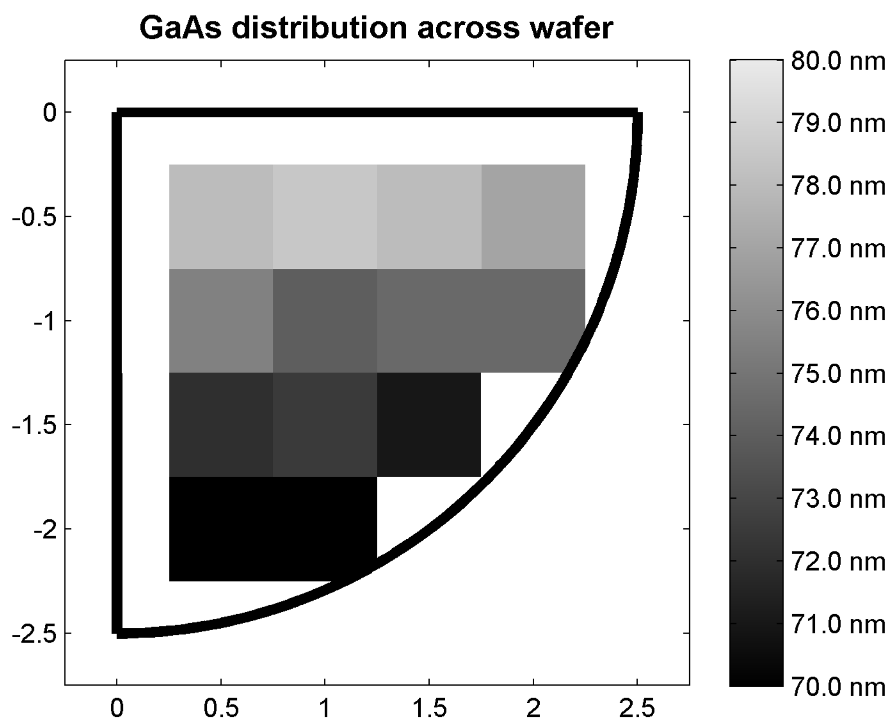

Figure 5.5: *Results of curve fittings for GaAs.*

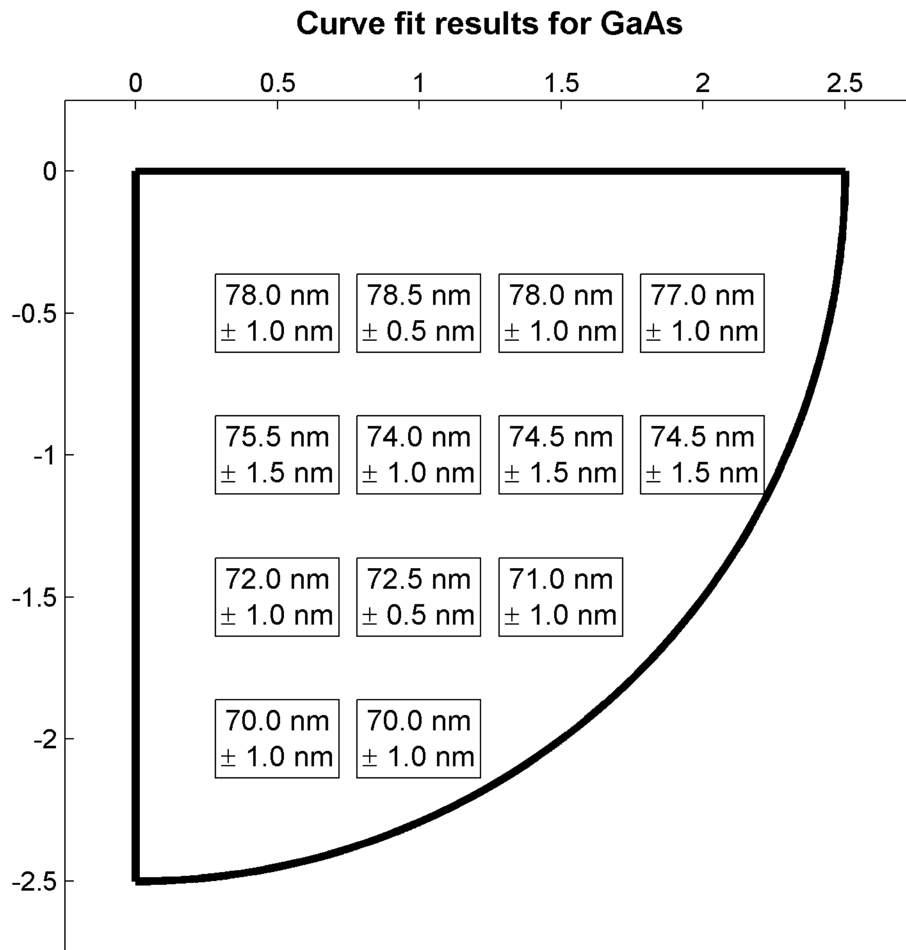

Figure 5.6: *Results of curve fittings for GaAs with uncertainties.*

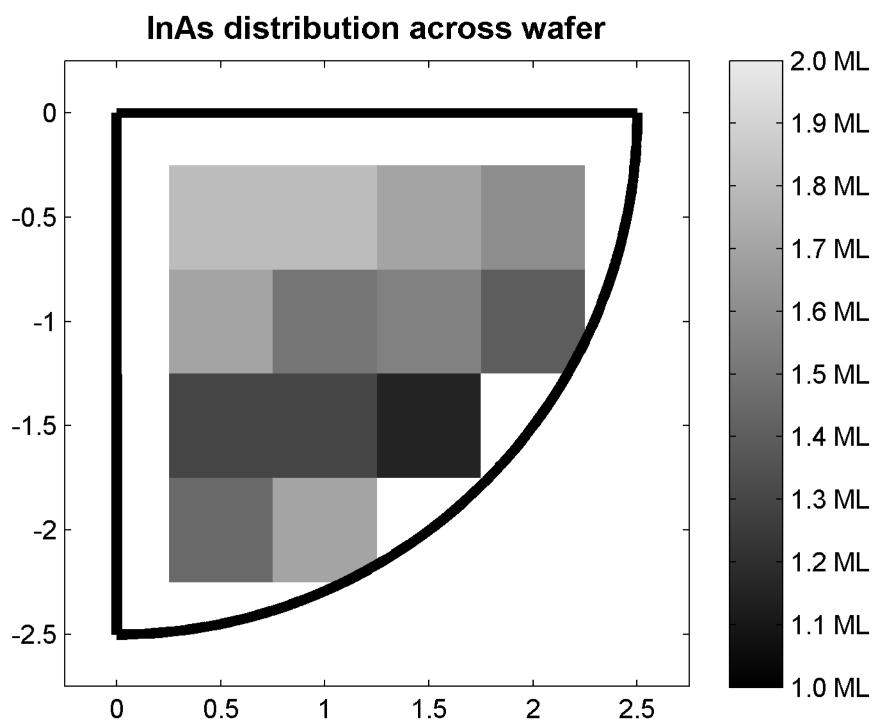

Figure 5.7: *Results of curve fittings for InAs.*

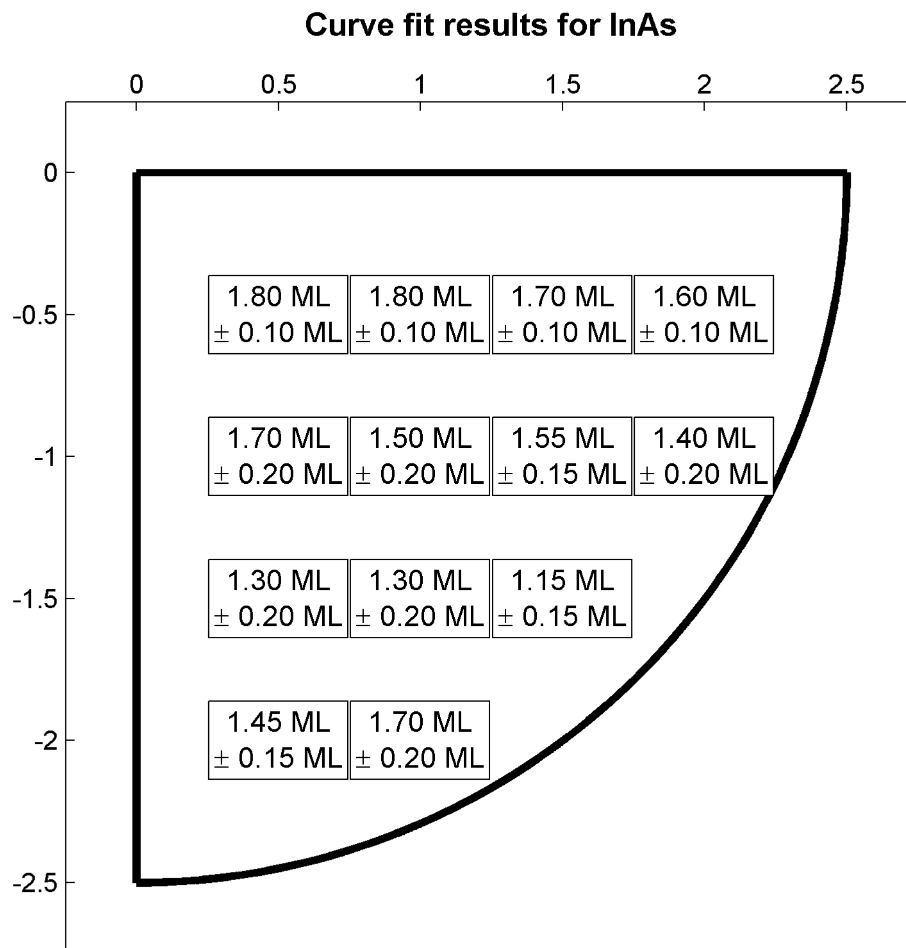

Figure 5.8: *Results of curve fittings for InAs with uncertainties.*

5.3 Estimated superlattice thickness

The superlattice thickness was estimated based on the satellite peaks in the measurement results. This was done by creating a plot with the peak order on the x axis and the $2\sin\omega/\lambda$ of the peak on the y axis (where ω is the measured angle of the peak and λ is the x-ray wavelength of 0.15406 nm). A straight line was fitted to this curve. Then the superlattice thickness is the slope of this line. The results can be seen in table 5.4 and figure 5.9.

Table 5.4: *Estimated superlattice thickness.*

Measurement	Superlattice thickness
001	82.18
002	81.69
003	81.31
004	81.02
005	78.82
006	77.92
007	77.43
008	77.85
009	75.03
010	77.82
011	73.92
012	73.54
013	73.30

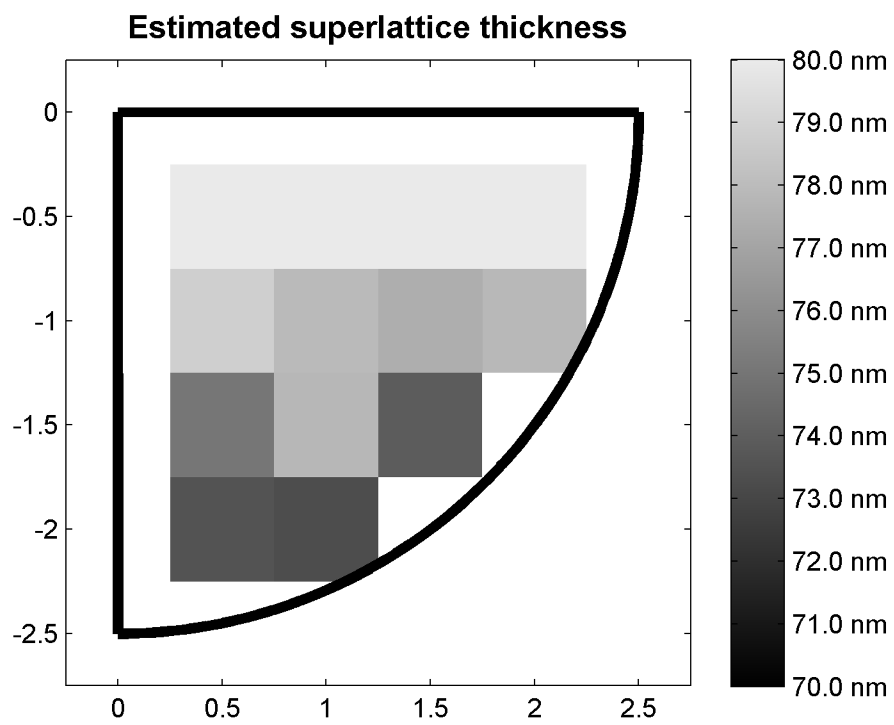

Figure 5.9: *Estimated superlattice thickness.*

5.4 Discussion

The GaAs thicknesses found in the curve fittings are in the range of 74.3 nm $\pm$4.3 nm. This is a change of $\pm$5.2%, slightly larger than the variation seen in the flux simulation which is $\pm$4.2% (see section 4.1). The GaAs curve fit results seem to exhibit a gradient similar to the one seen in the flux density simulation in figure 4.2.

It can be seen from figure 5.8 that the measured InAs thickness in the 001 measurement spot is significantly higher than the thicknesses in the 008 and 011 spots. This suggests there is a gradient in InAs thicknesses across this wafer in the same direction as the one seen in figure 4.1. The InAs thicknesses found in the curve fittings are in the range of 1.48 ML $\pm$0.33 ML, or $\pm$22%. This variation is significantly larger than the variation seen in the In flux simulation which is $\pm$3.4%. Also the InAs thicknesses seen are significantly lower than the nominal thickness, which is about 2.0 ML.

The quantum dot wetting layer for the InAs layers is expected to be about 1.4 ML $\pm$ 0.4 ML thick[19]. The results from the curve fittings are within this range, which is a strong indicator that there are quantum dots on the surface of the bottom InAs layer and that it is the wetting layer that is seen in the x-ray diffraction results. As more InAs is deposited the quantum dots increase in size and density and will eventually cover most of the surface, meaning they may start to affect the x-ray diffraction curve. This might explain the large variation in the measured InAs thickness.

The measured superlattice thicknesses seem to vary in the same direction as the measured GaAs thickesses. This is because most of the superlattice consists of GaAs, thus most of the variation in the superlattice thickness will be due to variations in the GaAs thickness.

Chapter 6

Conclusion

A InAs/GaAs heterostructure with nominal thicknesses as shown in figure 6.1 was studied. This sample had been grown by MBE without rotation, which means that the thicknesses of the GaAs and InAs layers are expected to exhibit a gradient across the wafer.

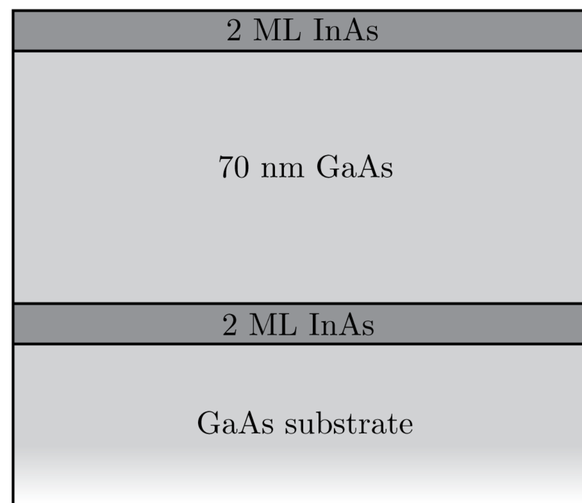

Figure 6.1: *A schematic drawing of the basic structure studied in this thesis.*

XRD measurements were done on multiple locations across this sample. Curve fittings were made on basis of these measurements, and it was found that the variation of GaAs thicknesses across the sample is roughly as expected. It was also found that the InAs bottom layer was significantly thinner than the nominal value and that the variation in InAs thickness was much larger than the variation seen in the MBE flux simulation. This is a strong

indication that there are quantum dots on the sample, and that the quantum dots do not contribute to the XRD signal as a thin film with an average InAs content.

Several simulations were also made to evaluate the effects of segregation and intermixing on the XRD curve. The main findings from these simulations were:

- Segregation of the bottom InAs layer does not cause a significant change in the XRD curve.
- Intermixing does lead to a significant change in the XRD curve, because it leads to an increase in the total amount of GaAs in the InAs/GaAs bilayer structure.
- When the bottom InAs/GaAs is made less abrupt, the diffraction peaks become weaker.

For future studies, the following suggestions are made:

- Samples without the InAs top layer could be made to study whether the lack of an InAs top layer affects the XRD curve.
- Simulations and curve fittings could be made where the strain relaxation is considered when calculating the thickness of the InAs layers.
- The surface of samples with a gradient in the InAs thickness could be studied with atomic force microscopy to find whether there are quantum dots on the surface and if the density and size of quantum dots vary depending on the location on the sample.

Bibliography

[1] W. Shockley and H. J. Queisser. Rocking curve peak shift in thin semiconductor layers. *Journal of Applied Physics*, volume 32, pages 510–519 (1961).

[2] A. Luque and A. Martí. Increasing the efficiency of ideal solar cells by photon induced transitions at intermediate levels. *Physical Review Letters*, volume 78, pages 5014–5017 (1997).

[3] L. Cuadra, A. Martí, and A. Luque. Present status of intermediate band solar cell research. *Thin Solid Films*, volume 451-452, pages 593–599 (2004).

[4] A. Martí, L. Cuadra, and A. Luque. Design constraints of the quantum-dot intermediate band solar cell. *Physica E*, volume 14, pages 150–157 (2002).

[5] J. T. Ng, U. Bangert, and M. Missous. Formation and role of defects in staced large binary inas/gaas quantum dot structures. *Semiconductor Science and Technology*, volume 22 (2007).

[6] B. G. Streetman and S. K. Banerjee. *Solid State Electronic Devices*. Pearson Education Inc., 6th edition (2006).

[7] M. Mansfield and C. O'Sullivan. *Understanding Physics*. Praxis Publishing Ltd (1998).

[8] M. A. Green. Third generation photovoltaics: Ultra-high conversion efficiency at low cost. *Progress in Photovoltaics: Research and Applications*, volume 9, pages 123–135 (2001).

[9] M. A. Green. *Solar Cells*. The University of New South Wales (1998).

[10] A. Martí, N. López, E. Antolín, E. Cánovas, C. Stanley, C. Farmer, L. Cuadra, and A. Luque. Novel semiconductor solar cell structures:

The quantum dot intermediate band solar cell. *Thin Solid Films*, volume 511-512, pages 638–644 (2006).

[11] P. C. Hemmer. *Kvantemekanikk*. Tapir Akademisk Forlag, 5th edition (2005).

[12] R. Waser, editor. *Nanoelectronics and Information Technology*. WILEY-VCH Verlag GmbH & Co. KGaA, 2nd edition (2005).

[13] O. Manasreh. *Semiconductor Heterojunctions and Nanostructures*. The McGraw-Hill Companies, Inc., 1st edition (2005).

[14] C. Kittel. *Introduction to Solid State Physics*. John Wiley & Sons, Inc., 8th edition (2005).

[15] E. Selvig. *Molecular beam epitaxial growth and characterization of GaInAsSb/AlGaAsSb mid-infrared laser structures*. Dr.Ing. thesis, NTNU (2004).

[16] T. E. Jenkins. *Semiconductor Science*. Prentice Hall International (UK) Limited, 1st edition (1995).

[17] M. Quirk and J. Serda. *Semiconductor Manufacturing Technology*. Pearson Education Inc. (2001).

[18] C. R. Wie. Detalied balance limit of efficiency of p-n junction solar cells. *Journal of Applied Physics*, volume 66, pages 985–988 (1989).

[19] T. Reenaas. Private communication.

Appendix A

Appendix

A.1 Source code for wafer flux simulations

```
function flux_sim
    function result = simulate(res_sim, l_wafer, r_0, shift_d)
        % simulate(res_sim, r_wafer, r_0, shift_d)
        % Simulates the gas flux across the surface of a substrate.
        % res_sim = resolution of simulation,
        % in number of points along x and y axis
        % l_wafer = length along one side of substrate.
        % r_0 = distance from source to center of substrate.
        % shift_d = rotation of substrate in degrees.

        % Create simulation
        sub_sim = zeros(res_sim, res_sim);
        for i = 1:res_sim
            for j = 1:res_sim
                x = ((i - ((res_sim+1)/2))/res_sim)*l_wafer;
                y = ((((res_sim+1)/2) - j)/res_sim)*l_wafer;
                mag = sqrt(x^2 + y^2);
                deg = atand(y/x);
                if (x < 0)
                    deg = 180 + deg;
                elseif (y < 0)
                    deg = 360 + deg;
                end
                x = mag*cosd(deg + shift_d);
                y = mag*sind(deg + shift_d);
                val = (r_0^2)/(r_0^2 + x^2 + y^2 + 2*y*r_0*cosd(57));
                rel_change = (val - 1)*100;
                sub_sim(((i - 1)*res_sim) + j) = rel_change;
            end
        end
```

```
    result = sub_sim;
end

res_edge = 10000; % Number of points drawn along curved edge of
                        % wafer. The higher, the smoother the wafer
                        % edge becomes.
    res_wafersim = 1500; % The resolution of the simulation.
                        % Note: The higher, the longer the simulation
                        % will take to calculate!
r_wafer = 2.50; % The radius of the wafer.
r_0 = 40.00; % The length from source to center of wafer.

% Define edge of wafer.
edge_x = zeros(1, res_edge+1);
edge_y = zeros(1, res_edge+1);
for k = 0:res_edge
    curr_rad = (2.00 - (k/res_edge)*0.50)*pi;
    edge_x(k+1) = r_wafer*cos(curr_rad);
    edge_y(k+1) = r_wafer*sin(curr_rad);
end

% Calculate outline of wafer.
frame_x = [0 edge_x 0];
frame_y = [0 edge_y 0];

% Calculate polygon to cover anything beyond curved edge.
curve_x = [ 2*r_wafer 2*r_wafer r_wafer edge_x -2*r_wafer ...
                                            -2*r_wafer 2*r_wafer];
curve_y = [-2*r_wafer 2*r_wafer 2*r_wafer edge_y -r_wafer ...
                                            -2*r_wafer -2*r_wafer];

    % Simulate and draw results twice. First for In, then for Ga, then for
    % As, and finally for the average of Ga and As.
for l=1:2
    % Create new, blank figure to draw on.
    figure();

    % Set values for simulation
    if l == 1
        sim_title = 'In␣flux␣distribution␣across␣wafer';
        fname = 'in_flux';
        angle = 112.50;
    elseif l == 2
        sim_title = 'Ga␣flux␣distribution␣across␣wafer';
        fname = 'ga_flux';
        angle = 202.50;
    end

    % Simulate.
```

```
        wafer_sim = simulate(res_wafersim, r_wafer, r_0, angle);

        % Draw results.
        colormap(gray);
        imagesc([0.00 r_wafer], [0.00 -r_wafer ], wafer_sim, [-5 5]);
        colorbar('EastOutside', 'YTickLabel', {'-5.00%', '-4.00%', ...
                                            '-3.00%','-2.00%', ...
                                            '-1.00%', '0.00%', ...
                                            '1.00%', '2.00%', ...
                                            '3.00%', '4.00%', ...
                                            '5.00%'});
        title(sim_title, 'FontWeight','bold', 'FontSize', 12);

        % Set axes.
        axis manual
        axis equal
        axis([-(r_wafer/10) (11*r_wafer/10) -(11*r_wafer/10) (r_wafer/10)])
        set(gca, 'YDir', 'normal')
        hold on

        % Cover anything outside wafer.
        patch(curve_x,curve_y,[1.0 1.0 1.0], 'EdgeColor', 'none')

        % Draw outline of wafer.
        line(frame_x, frame_y, 'LineWidth', 3.0, 'Color', [0 0 0])

        % Draw cross in center.
        line('Xdata', [1.25, 1.25], 'Ydata', [-1.00, -1.50], ...
                                'LineWidth', 1.5, ...
                                'Color', [1 1 1]);
        line('Xdata', [1.00, 1.50], 'Ydata', [-1.25, -1.25], ...
                                'LineWidth', 1.5, ...
                                'Color', [1 1 1]);

        % Dimensions of figure in cm.
        x_dim = 13;
        y_dim = 11;

        % Save figure to file (both as pdf and png).
        set(gcf,'paperunits','centimeters');
        set(gcf,'papersize',[x_dim, y_dim])
        set(gcf,'paperposition',[0,0,x_dim, y_dim])
        saveas(gcf, strcat(fname, '.pdf'));
        set(gcf,'renderer','zbuffer');
        print(gcf, '-r300', '-dpng', strcat(fname, '.png'));
    end
end
```